

# Unlocking The Potential of Adaptive Attacks on Diffusion-Based Purification

Andre Kassis    Urs Hengartner    Yaoliang Yu  
Cheriton School of Computer Science, University of Waterloo, Canada

## Abstract

*Diffusion-based purification (DBP) is a defense against adversarial examples (AEs), amassing popularity for its ability to protect classifiers in an attack-oblivious manner and resistance to strong adversaries with access to the defense. Its robustness has been claimed to ensue from the reliance on diffusion models (DMs) that project the AEs onto the natural distribution. We revisit this claim, focusing on gradient-based strategies that back-propagate the loss gradients through the defense, commonly referred to as “adaptive attacks”. Analytically, we show that such an optimization method invalidates DBP’s core foundations, effectively targeting the DM rather than the classifier and restricting the purified outputs to a distribution over malicious samples instead. Thus, we reassess the reported empirical robustness, uncovering implementation flaws in the gradient back-propagation techniques used thus far for DBP. We fix these issues, providing the first reliable gradient library for DBP and demonstrating how adaptive attacks drastically degrade its robustness. We then study a less efficient yet stricter majority-vote setting where the classifier evaluates multiple purified copies of the input to make its decision. Here, DBP’s stochasticity enables it to remain partially robust against traditional norm-bounded AEs. We propose a novel adaptation of a recent optimization method against deepfake watermarking that crafts systemic malicious perturbations while ensuring imperceptibility. When integrated with the adaptive attack, it completely defeats DBP, even in the majority-vote setup. Our findings prove that DBP, in its current state, is not a viable defense against AEs.*

## 1. Introduction

ML classifiers are sensitive to *Adversarial Examples (AEs)* generated via imperceptible perturbations to benign inputs typically using gradient-based optimizations, causing misclassification [20, 46]. Common defenses are *Adversarial Training* and *Pre-processing*. The former retrains classifiers on AEs to increase their robustness [34, 63]. Yet, it is vulnerable to unseen attacks and re-training is often prohibitive [52]. The latter avoids retraining and is attack-

agnostic, applying pre-classification operations to the input, typically involving non-differentiable layers or stochasticity, yielding *obfuscated* (incorrect or incomputable) gradients [4, 11, 16, 21, 38, 55, 57, 58]. Still, it is vulnerable to adaptive attacks [47]: Stochastic defenses lack sufficient randomness [18, 40], and non-differentiable layers can be approximated [3]. A sub-class of *Pre-processing* is *Purification*, which uses generative models [24, 41, 44] to project AEs onto the natural manifold. In addition to its vulnerabilities as a *Pre-processing* defense, early generative models lacked sufficient computational power [19] and impacted the sample quality [30], preventing correct classification.

Recently, a variant of *Purification*, namely *Diffusion-based Purification (DBP)* [36, 49], which relies on diffusion models (DMs) [43, 45], has become the *SOTA* due to its theoretical foundations, inspiring numerous works [6–8, 37, 51, 53, 56, 62, 64]. Purification is performed by solving the reverse stochastic differential equation (*SDE*) that characterizes DMs. Gaussian noise is first introduced to diminish malicious interruptions. *DBP* then iteratively reconstructs the input by solving this *SDE*, gradually eliminating the noise. As DMs possess unparalleled data modeling abilities [15, 48], *DBP* can employ increased randomness. Its iterative reverse pass ensures that, at each step, the sample is from the marginal **natural** distribution (i.e., that is obtained by introducing noise into natural inputs, with an amount corresponding to that step). Under this assumption, adversarial optimizations are subject to the constraint that purified samples are from the natural distribution. Thus, unlike previous defenses, *DBP* would result in a plain surface around the purified *AE* wherein the correct label is immutable as all neighboring *DBP* outputs are also restricted to the natural distribution and will be classified correctly. This renders optimizations impossible under a restricted perturbation budget (as the gradients are non-existent).

We scrutinize the *DBP* paradigm, refuting the hypothesis regarding its robustness rooted in the ability to perform projection onto the natural manifold. This hypothesis is itself paradoxical as it relies on the correct behavior of the score model  $s_\theta$  used by the *DM* to mimic the gradients of the marginal distributions. Yet,  $s_\theta$  itself is an *ML* system with imperfections that can be exploited. In §4.1, we prove that,

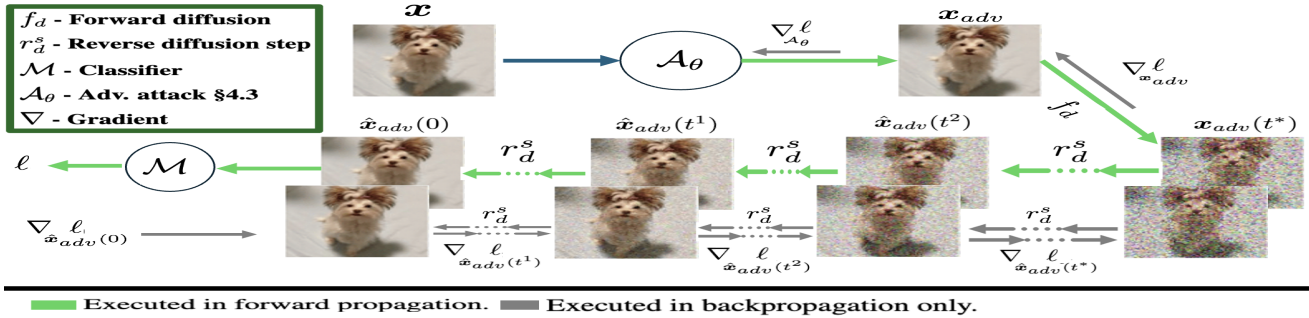


Figure 1. Overview of **DiffGrad**.  $\mathbf{x}$  is given to the attack  $\mathcal{A}_\theta$  that iteratively optimizes it to generate the AE  $\mathbf{x}_{adv}$ . At each iteration, *DBP* is invoked, propagating  $\mathbf{x}_{adv}$  to the purified  $\hat{\mathbf{x}}_{adv}(0)$  that is then given to  $\mathcal{M}$  while storing each intermediate  $\hat{\mathbf{x}}_{adv}(t)$  (bottom replicas) encountered during *DBP*'s reverse pass (see §2) but without saving any graph dependencies. Our efficient backpropagation uses the stored samples: Starting from  $t = -dt$  (where  $dt$  is the **negative** step size used in the reverse pass), each  $\hat{\mathbf{x}}_{adv}(t)$  is used to recompute  $\hat{\mathbf{x}}_{adv}(t+dt)$ , retrieving only the required dependencies. Then, we recursively obtain the gradient w.r.t.  $\hat{\mathbf{x}}_{adv}(t)$  from the gradients w.r.t.  $\hat{\mathbf{x}}_{adv}(t+dt)$  using this recovered sub-graph (see §4.2). Finally, gradients are backpropagated in a standard manner from  $\hat{\mathbf{x}}_{adv}(t^*)$  to  $\mathcal{A}_\theta$  to update  $\hat{\mathbf{x}}_{adv}$ .

effectively, an attack that back-propagates the exact gradients from the classifier's output to the input targets the score model rather than the classifier, forcing it to generate samples from an adversarial distribution. Hence, the entirety of the theory behind *DBP* no longer holds.

Thus, in §4.2, we investigate *DBP*'s previously reported robustness [36, 49, 56, 64], attributing it to flawed implementations of gradient backpropagation. As computing *DBP*'s gradients is memory-exhaustive [31, 36], prior works use approximations [3, 32], or implement efficient back-propagation of the exact gradients [26, 33] via checkpointing [9]. Yet, subtle errors and unaddressed factors will result in discrepancies between the actual and obtained gradients. We propose fixes, providing **DiffGrad**—the first module for correctly computing *DBP*'s gradients (see Fig. 1). Our experiments in §5 reveal *DBP* is significantly impacted by adaptive attacks under standard optimization methods (e.g., *AutoAttack-l<sub>∞</sub>* [12]), driving its robustness below 21% in the common *empirical* setting [26, 31, 36, 49], where the input is purified via a *single* random path.

We then explore a stricter, less efficient setup that purifies the sample through multiple paths, taking the majority vote over the classifier's decisions, and find *DBP* retains **partial** resistance. As we established the inefficacy of intermediate projections, we conclude this is due to *DBP*'s increased stochasticity over previous defenses: common adversarial perturbations that introduce large changes to *individual* pixels are diluted and may not impact most paths as desired. Hence, defeating *DBP* in this setup requires systemic modifications that affect many pixels simultaneously while remaining invisible. In §4.3, we propose a novel adaptation integrating **DiffGrad** with a recent adversarial strategy [27] from the watermarking domain that crafts such low-frequency perturbations, accounting for the links between neighboring pixels. This technique, we term *LF* (low-frequency), prevents sporadic changes, also allowing for slightly increased budgets without violating visual

constraints, defeating *DBP* in this more challenging setting.

Our contributions are: (i) Analytically scrutinizing adaptive attacks on *DBP*, showing they nullify theoretical claims regarding its robustness. (ii) Identifying and addressing flaws in the backpropagation methods previously used in adaptive attacks, enabling reliable evaluations and demonstrating significantly degraded performance of *DBP*. (iii) Evaluating the *practical* advantages of a stricter *majority-vote* setup for *DBP*. (iv) Proposing and adapting low-frequency (*LF*) optimizations to adversarially attacking *DBP*, achieving unprecedented success even in the *majority-vote* setting. (v) Availability: existing *DBP* implementations and attacks lack generalizability, with code specific to the methods from the corresponding papers [26, 36, 49]. We provide *DiffBreak*<sup>1</sup>—the first toolkit that allows defending any classifier with *DBP* and evaluating it under various optimization methods, including our novel *LF*, using our reliable **DiffGrad** module for backpropagation.

Extensive evaluations on *ImageNet* and *CIFAR-10* prove our methods defeat *DBP*, bringing its robustness to ~0%, outperforming previous works by a large margin.

## 2. Background & Related Work

**Diffusion models (DMs)**. [43, 45] allow learning a process to model a distribution  $p$  on  $\mathbb{R}^d$  by inverting the procedure through which inputs diffuse in time into pure noise. *DMs* have two stochastic processes of interest. The forward pass transforms samples into pure Gaussians and is represented by the below *SDE* (for an infinitesimal time step  $dt > 0$ ):

$$d\mathbf{x} = \mathbf{f}(\mathbf{x}, t)dt + g(t)d\mathbf{w}. \quad (1)$$

*eq. (1)* describes a stochastic integral whose solution up to  $t^* \in [0, 1]$  gives  $\mathbf{x}(t^*)$ . Here,  $\mathbf{f}: \mathbb{R}^d \times \mathbb{R} \rightarrow \mathbb{R}^d$  is the drift,  $\mathbf{w}: \mathbb{R} \rightarrow \mathbb{R}^d$  is a Wiener process, and  $g: \mathbb{R} \rightarrow \mathbb{R}$  is the diffusion coefficient. We focus on **VP-SDE**, which is the most common *DM* for *DBP* [36, 49, 56]. Yet, our insights

<sup>1</sup><https://github.com/andrekkassis/DiffBreak.git>

generalize to all *DMs*. For a full review of *DMs*, see [45]. In **VP-SDE**,  $\mathbf{f}(\mathbf{x}, t) = -\frac{1}{2}\beta(t)\mathbf{x}(t)$  and  $g(t) = \sqrt{\beta(t)}$ , where  $\beta(t)$  is a noise scheduler outputting small positive constants. These  $\mathbf{f}$  and  $g$  yield a closed-form solution:

$$\mathbf{x}(t^*) = \sqrt{\alpha(t^*)}\mathbf{x} + \sqrt{1 - \alpha(t^*)}\epsilon \quad (2)$$

for  $\epsilon \sim \mathcal{N}(\mathbf{0}, \mathbf{I}_d)$  and  $\alpha(t) = e^{-\int_0^t \beta(s) ds}$ . With proper parameters, we have  $\mathbf{x}(1) \sim \mathcal{N}(\mathbf{0}, \mathbf{I}_d)$ . Thus, a process that inverts eq. (1) from  $t^* = 1$  to 0 allows generating samples in  $p$  from random noise. Due to Anderson [2], the reverse pass is known to be a stochastic process with:

$$d\hat{\mathbf{x}} = [\mathbf{f}(\hat{\mathbf{x}}(t), t) - g^2(t)\nabla_{\hat{\mathbf{x}}(t)} \log p_t(\hat{\mathbf{x}}(t))]dt + g(t)d\bar{\mathbf{w}}. \quad (3)$$

Defining  $\hat{\mathbf{x}}(t^*) := \mathbf{x}(t^*)$ , the process  $d\hat{\mathbf{x}}$  travels back from  $t^*$  to 0. Here,  $dt$  is a **negative** time step and  $\bar{\mathbf{w}}(t)$  is a reverse-time Wiener process. Denote by  $p(\mathbf{x})$  the probability of  $\mathbf{x}$  under  $p$  and by  $p_{0t}(\tilde{\mathbf{x}}|\mathbf{x})$  the conditional probability of the output of the forward pass  $\mathbf{x}(t)$  at step  $t$  being  $\tilde{\mathbf{x}}$  given  $\mathbf{x}(0) = \mathbf{x}$ . Then, the marginal distribution density of  $p_t$  from eq. (3) is  $p_t(\tilde{\mathbf{x}}) = \int p(\mathbf{x})p_{0t}(\tilde{\mathbf{x}}|\mathbf{x})d\mathbf{x}$ , with  $p_0 \equiv p$ . Solving eq. (3) requires the **score**  $\nabla_{\hat{\mathbf{x}}(t)} \log p_t(\hat{\mathbf{x}}(t))$ , which can be approximated via a trained network  $s_\theta$  s.t.  $s_\theta(\hat{\mathbf{x}}(t), t) \approx \nabla_{\hat{\mathbf{x}}(t)} \log p_t(\hat{\mathbf{x}}(t))$  at any point [45]. Accordingly:

$$d\hat{\mathbf{x}} = -\frac{1}{2}\beta(t)[\hat{\mathbf{x}}(t) + 2s_\theta(\hat{\mathbf{x}}(t), t)]dt + \sqrt{\beta(t)}d\bar{\mathbf{w}}. \quad (4)$$

As no closed-form solution exists, the process runs iteratively over **discrete** negative steps  $dt$ . Starting from  $t^*$ ,  $d\hat{\mathbf{x}}$  is calculated at each  $i = \lfloor \frac{t}{dt} \rfloor$ , until  $t = 0$ . This *continuous-time DM* describes a stochastic integral (despite the discretized implementations). An alternative, *Denosing diffusion probabilistic modeling (DDPM)* [25, 43], considers a *discrete-time DM*. Effectively, the two are equivalent [45]. **DBP**. [36, 49, 56, 60] performs purification by diffusing each input  $\mathbf{x}$  until optimal time  $t^*$  that preserves class semantics while still diminishing malicious interruptions.  $\mathbf{x}(t^*)$  is then given to the reverse pass, reconstructing a clean  $\hat{\mathbf{x}}(0) \approx \mathbf{x}$  s.t.  $\hat{\mathbf{x}}(0) \sim p$  for correct classification.

*DBP* has been studied as an *empirical* [8, 36, 37, 49, 62] and a certifiable [6, 7, 53, 56, 64] defense. Since the certified radii are typically insufficient to ensure practical resistance, we focus on the *empirical* setting. While *DBP*'s robustness has been questioned in the past [26, 31, 33], these papers and other works proposing extensions to *DBP* [8, 37, 59, 62] fail to gauge the power of adaptive attacks due to persisting fallacies (see §4.2). We address these issues for the first time and provide a reliable evaluation of *DBP*.

### 3. Threat Model

Below, we formulate the problem of generating *AEs* against *DBP*-defended classifiers, describing the relevant parties:

**Attacker. Goal:** Given  $\mathbf{x} \in \mathbb{R}^d$  with true label  $y$ , classifier (model)  $\mathcal{M}$ , and preprocessing defense  $G$  (when no defense is used,  $G \equiv Id$ ), attackers aim to generate a visually similar

$\mathbf{x}_{adv}$  s.t.  $\mathcal{M}(G(\mathbf{x}_{adv})) \neq y$ . Crafting  $\mathbf{x}_{adv}$  is formalized as:

$$\mathbf{x}_{adv} = \arg \min_{\mathcal{D}(\mathbf{x}', \mathbf{x}) \leq \epsilon_{\mathcal{D}}} \mathbb{E}[\ell_G^{\mathcal{M}}(\mathbf{x}', y)]$$

for loss  $\ell_G^{\mathcal{M}}$ . Typically,  $\ell_G^{\mathcal{M}}(\mathbf{x}, y) = \ell(\mathcal{M}(G(\mathbf{x})), y)$ , where  $\ell$  is a loss over  $\mathcal{M}$ 's output that captures the desired outcome. For instance,  $\ell(\mathcal{M}(G(\mathbf{x})), y)$  can be chosen as the probability that the classifier's output label is  $y$ , which we strive to minimize.  $\mathcal{D}$  is a distance metric that ensures similarity if kept below some  $\epsilon_{\mathcal{D}}$ . These *untargeted* attacks are the focus of many works [35, 36, 38, 49]. The expected value accounts for potential stochasticity in  $G$  (e.g., *DBP*). **Capabilities:** We focus on *DBP*-defended classifiers ( $G \equiv \overline{DBP}$ ), assuming white-box access to  $\mathcal{M}$ 's and *DBP*'s parameters, but not the randomness at each *DBP* invocation (see §2). This is realistic since *DBP*'s practicality is based on utilizing off-the-shelf *DMs*, while  $\mathcal{M}$  can be leaked or replicated [39, 42]. They can access advanced hardware as such systems are available for relatively low costs [1].

**Defender.** They wish to ensure their classifier's fidelity using *DBP*. Most works assume defenders obtain  $\mathbf{x}$ 's label by invoking *DBP* once, arriving at a single purified  $\hat{\mathbf{x}}(0)$  forwarded to  $\mathcal{M}$ . Attackers perturb  $\mathbf{x}$  aiming for a **single** misclassification. Yet, as recently proposed by Xiao et al. [56], defenders may generate several copies  $\hat{\mathbf{x}}(0)$  via different random paths, taking the majority vote over  $\mathcal{M}$ 's decisions. We term this the *majority-vote (MV)* setting and refer to the former, commonly dubbed *empirical*, as *single-purification (SP)*. *MV* might be infeasible in high-throughput systems unless extensive resources are available but may achieve better robustness as *DBP*'s stochasticity makes *AEs* less likely to impact all copies [33]. We study both settings.

## 4. Revisiting Adaptive Attacks on *DBP*

Here, we study the efficacy of gradient-based attacks. In §4.1, we theoretically establish that adaptive attacks invalidate *DBP*'s principles. In §4.2, we reconcile this with previous findings of *DBP*'s robustness, attributing them to flaws in the used backpropagation logic and propose fixes. Finally, present a low-frequency strategy that generates stealthy systemic adversarial perturbations of larger magnitudes to defeat *DBP* even under the strict *MV* setup.

### 4.1. Robustness in Perspective

*DBP*'s robustness is primarily attributed to its ability to project the purified  $\hat{\mathbf{x}}(0)$  onto the natural manifold: Since  $s_\theta \approx \nabla \log p_t$ ,  $\{\mathbf{x}(t)\}_{t \in [0,1]}$  and  $\{\hat{\mathbf{x}}(t)\}_{t \in [0,1]}$  follow the same marginal distributions [2], yielding  $\hat{\mathbf{x}}(0) \sim p$ . Specifically, under *DBP* Xiao et al. [56] show that given input  $\mathbf{x}$ :

$$\Pr(\hat{\mathbf{x}}(0)|\mathbf{x}) \propto p(\hat{\mathbf{x}}(0)) \cdot e^{-\frac{\alpha(t^*)\|\hat{\mathbf{x}}(0) - \mathbf{x}\|_2^2}{2(1 - \alpha(t^*))}}$$

where  $p$  is the density of the natural distribution, and  $\alpha(t^*)$  is the same from eq. (2). Thus, *DBP* should ideally protect

against AEs since for any purified sample  $\hat{x}(0)$  that is also adversarial, the probability of it being outputted by *DBP* is extremely low since such inputs are unnatural (i.e.,  $p(\hat{x}(0))$  is low). These guarantees, however, assume *DBP*'s reverse process models the natural distribution. Yet, skilled adversaries may attempt to influence it s.t. the outputs, given  $\mathbf{x}$ , are from another distribution restricted to samples whose assigned label by  $\mathcal{M}$  differs from the ground truth  $y$  of  $\hat{x}$ . This is possible since the score model  $s_\theta$  is itself an *ML* model susceptible to adversarial attacks that modify  $\mathbf{x}$ .

We demonstrate how the attack that propagates copies of  $\mathbf{x}$  through *DBP* and back-propagates the loss gradients, taking their average to perform gradient descent, achieves this, effectively targeting  $s_\theta$ , rather than the classifier. This invalidates all guarantees of *DBP* and reveals it merely replaces the target *ML* system of the adversarial optimization. Realizing  $s_\theta$  can be influenced by  $\mathbf{x}$ , we part company with existing work, denoting  $s_\theta$ 's parameters by  $\theta_{\mathbf{x}}^t$  to capture their dependence (at all reverse steps) on  $\mathbf{x}$ . Recalling that *DBP* generates an output distribution, our objective is to perturb  $\mathbf{x}$  s.t. the values assigned to the parameters of the reverse process  $\theta_{\mathbf{x}}^t$  maximize  $\Pr(\neg y|\mathbf{x})$ . We make a standard assumption  $\Pr(\neg y|\mathbf{x}) \in \mathcal{C}^2$  as this is typically easily satisfiable, allowing us to use gradient-based methods.

$\Pr(\neg y|\mathbf{x})$  relies on the hidden distribution of the parameters  $\theta_{\mathbf{x}}^t$ , and the distribution of  $\hat{x}_{t^*:0}$ , which denotes the samples (random variables)  $\{\hat{x}(t)\}_{t \in [0, t^*]}$  along the reverse path, dictating the purified  $\hat{x}(0)$  forwarded to the classifier. Yet, following *eq. (4)*, the parameters  $\theta_{\mathbf{x}}^t$  are set once  $\hat{x}(t)$  is selected since  $s_\theta$  is pretrained and the remainder of its parameters immutable. Hence, we may consider the intermediate outputs  $\hat{x}_{t^*:0}$  as the only optimizable hidden distribution based on  $\mathbf{x}$ . Thus, the objective is:

$$\begin{aligned} \Pr(\neg y|\mathbf{x}) &= \int \Pr(\neg y, \hat{x}_{t^*:0}|\mathbf{x}) d\hat{x}_{t^*:0} \\ &= \int \Pr(\neg y|\hat{x}_{t^*:0}, \mathbf{x}) \Pr(\hat{x}_{t^*:0}|\mathbf{x}) d\hat{x}_{t^*:0} \\ &= \int \Pr(\neg y|\hat{x}_{t^*:0}) p_{\theta_{\mathbf{x}}}(\hat{x}_{t^*:0}|\mathbf{x}) d\hat{x}_{t^*:0} \end{aligned}$$

where  $p_{\theta_{\mathbf{x}}}(\hat{x}_{t^*:0}|\mathbf{x})$  replaces  $\Pr(\hat{x}_{t^*:0}|\mathbf{x})$  to emphasize the dependence of the path  $\hat{x}_{t^*:0}$  on the intermediate parameters that are the effective targets of our optimization. The last transition holds since given  $\hat{x}(0)$  (i.e., the final sample of the *DBP* path  $\hat{x}_{t^*:0}$ ), the label probability assigned by the classifier depends only on this  $\hat{x}(0)$ , and the conditioning on  $\mathbf{x}$  can be omitted. For the same reason:

$$\Pr(\neg y|\mathbf{x}) = \int \Pr(\neg y|\hat{x}(0)) p_{\theta_{\mathbf{x}}}(\hat{x}_{t^*:0}|\mathbf{x}) d\hat{x}_{t^*:0}$$

ignoring previous steps. Since we assume  $\Pr(\neg y|\hat{x}(0)) \in \mathcal{C}^2$ , we may interchange the integral and gradient, yielding:

$$\nabla_{\mathbf{x}}[\Pr(\neg y|\mathbf{x})] = \int \Pr(\neg y|\hat{x}(0)) \nabla_{\mathbf{x}}[p_{\theta_{\mathbf{x}}}(\hat{x}_{t^*:0}|\mathbf{x})] d\hat{x}_{t^*:0}$$

where the last step is because  $\Pr(\neg y|\hat{x}(0))$  does not depend on  $\mathbf{x}$ , but only on  $\hat{x}(0)$  which is independent of  $\mathbf{x}$

(though its probability of being the final output of *DBP* is a function of  $\mathbf{x}$ ). Optimizing the objective relies on altering *DBP*'s output distribution alone, evident in its gradient where  $\Pr(\neg y|\hat{x}(0))$  assigned by the classifier is a constant with its gradient ignored. While we lack direct access to the gradients of the probabilistic paths above, we may still attempt to solve the optimization problem. Let  $\mathcal{M}(\mathbf{u})$  denote  $\mathcal{M}$ 's output on any sample  $\mathbf{u}$ . This is a vector containing the per-label probabilities s.t. its  $y^{\text{th}}$  cell is  $\mathcal{M}^y(\mathbf{u}) \equiv \Pr(y|\mathbf{u})$ . Thus, the required gradient can also be expressed as:

$$\begin{aligned} \nabla_{\mathbf{x}}[\Pr(\neg y|\mathbf{x})] &= \nabla_{\mathbf{x}} \left[ \int \Pr(\neg y|\hat{x}(0)) p_{\theta_{\mathbf{x}}}(\hat{x}_{t^*:0}|\mathbf{x}) d\hat{x}_{t^*:0} \right] = \\ &= \nabla_{\mathbf{x}} \left[ \mathbb{E}_{p_{\theta_{\mathbf{x}}}(\hat{x}_{t^*:0}|\mathbf{x})} [1 - \mathcal{M}^y(\hat{x}(0))] \right] = -\nabla_{\mathbf{x}} \left[ \mathbb{E}_{p_{\theta_{\mathbf{x}}}(\hat{x}_{t^*:0}|\mathbf{x})} [\mathcal{M}^y(\hat{x}(0))] \right] \end{aligned}$$

Yet, this expectation is over probabilistic paths whose randomness is due to the noise  $\epsilon$  of the forward pass and the Brownian motion  $d\bar{w}_t$  at each reverse step  $t$  that are independent. Hence, by the law of the unconscious statistician:

$$-\nabla_{\mathbf{x}} \left[ \mathbb{E}_{p_{\theta_{\mathbf{x}}}(\hat{x}_{t^*:0}|\mathbf{x})} [\mathcal{M}^y(\hat{x}(0))] \right] = -\nabla_{\mathbf{x}} \left[ \mathbb{E}_{p_r(\epsilon, d\bar{w}_{t^*}, \dots, d\bar{w}_0)} [\mathcal{M}^y(\hat{x}(0))] \right]$$

where  $p_r(\epsilon, d\bar{w}_{t^*}, \dots, d\bar{w}_0)$  denotes the joint distribution of the noise  $\epsilon$  and the Brownian motion vectors in the reverse pass. Note that  $\hat{x}(0)$  on the RHS denotes the output obtained by invoking the *DBP* pipeline with some assignment of these random vectors on the sample  $\mathbf{x}$ . As earlier, we can interchange the derivation and integration, obtaining:

$$-\mathbb{E}_{p_r(\epsilon, d\bar{w}_{t^*}, \dots, d\bar{w}_0)} \left[ \nabla_{\mathbf{x}} [\mathcal{M}^y(\hat{x}(0))] \right].$$

Let  $\mathbf{G}^{\mathbf{x}}$  denote the random variable that is assigned values from  $\nabla_{\mathbf{x}} \mathcal{M}^y(\hat{x}(0))$ , where  $\hat{x}(0)$  is as described above, and denote its covariance matrix by  $\Sigma_{\mathbf{G}^{\mathbf{x}}}$ . Essentially, we are interested in  $\mathbb{E}[\mathbf{G}^{\mathbf{x}}]$ . If we define  $\tilde{\nabla}_{\mathbf{x}}$  as:

$$\tilde{\nabla}_{\mathbf{x}} = \frac{1}{N} \sum_{n=1}^N \nabla_{\mathbf{x}} [\mathcal{M}^y(\hat{x}(0)_n)]$$

where each  $\hat{x}(0)_n$  is the output of *DBP* invoked with a certain random path  $(\epsilon^n, d\bar{w}_{t^*}^n, \dots, d\bar{w}_0^n) \stackrel{i.i.d.}{\sim} p(\epsilon, d\bar{w}_{t^*}, \dots, d\bar{w}_0)$  and  $N$  is a sufficiently large number of samples. Then due to the central limit theorem,  $\tilde{\nabla}_{\mathbf{x}} \rightarrow \mathcal{N}(\mathbb{E}[\mathbf{G}^{\mathbf{x}}], \frac{\Sigma_{\mathbf{G}^{\mathbf{x}}}}{N})$ . That is, propagating multiple copies through *DBP* and then averaging the loss gradients computes the required gradient for forcing *DBP* to alter its output distribution. The larger the number  $N$  of samples is, the lower the variance of the error, as can be seen above. Note that the adaptive attack operates exactly in this manner, assuming it uses  $\mathcal{M}^y$  as the loss it minimizes (but the soundness of the approach generalizes intuitively to any other loss with the same objective over the classifier's logits), proving our claim.

## 4.2. Precise *DBP* Gradients with DiffGrad

Our analysis challenges previous findings [26, 31, 33, 36, 49]. Thus, below, we investigate potential factors behind the

reported failure of the adaptive attack the **DiffGrad** module provided by our *DiffBreak* toolkit addresses. To distinguish *DBP*'s forward and reverse passes from the **propagation** through *DBP* (involving both passes) and gradient backpropagation, we restrict the terms forward and reverse passes to *DBP*'s stages and refer to its invocation and gradient calculation as forward and backward propagation. With  $\hat{\boldsymbol{x}}(t^*) := \boldsymbol{x}(t^*)$ , the reverse pass can be written recursively:

$$\hat{\boldsymbol{x}}(t+dt) = \hat{\boldsymbol{x}}(t) + d\hat{\boldsymbol{x}}(t) \quad (5)$$

with  $dt < 0$ , allowing us to view it as a chain of layers that operate on the outputs of one another. With that in mind, we can obtain the gradient of any function  $F$  of  $\hat{\boldsymbol{x}}(t+dt)$  w.r.t  $\hat{\boldsymbol{x}}(t)$  using the known rule from optimization theory:

$$\nabla_{\hat{\boldsymbol{x}}(t)} F = \nabla_{\hat{\boldsymbol{x}}(t)} \langle \hat{\boldsymbol{x}}(t+dt), \nabla_{\hat{\boldsymbol{x}}(t+dt)} F \rangle \quad (6)$$

yielding a recursive formula for the gradient of any loss w.r.t.  $\hat{\boldsymbol{x}}(t^*)$  (and trivially w.r.t.  $\boldsymbol{x}$  due to *eq. (2)*). While this is the basis of automatic differentiation, standard implementations fail for *DBP* due to the overhead of storing excessive graph dependencies between each  $\hat{\boldsymbol{x}}(t+dt)$  and  $\hat{\boldsymbol{x}}(t)$  to use for backpropagation.

An alternative is the **adjoint** method [32] that uses an additional *SDE* to approximate the *continuous-time DBP*'s gradients, and whose solution involves computations with the negations of the steps of reverse pass: Given the interval  $[t^*, 0]$ , the **adjoint** method operates on  $[0, -t^*]$ . Yet, in **VP-SDE**,  $t=0$  causes numerical explosions (see [45]). Thus, the process stops at some small  $t_e$  (typically  $10^{-5}$ ). The solver first sets  $t=t^*$  and updates it via  $t = \max(t+dt, t_e)$ . Previous works use the de-facto standard *torchsde* [32] library for *continuous-time SDE* that also provides the **adjoint** method. Our inspection reveals its **adjoint** method's code mishandles this nuance. While it does start from  $t=-t_e$ , it mistakenly updates it via  $t = \max(t+dt, -t^*)$ . Yet, from the update rule of the reverse pass above, we learn that upon the first update,  $t$  will be assigned an incorrect value that does not match that required by the **adjoint** process: Here,  $t$  will be set to  $t = -t_e + dt$ , while the correct assignment is  $t = dt$ . After this first update, all subsequent steps will be off by  $t_e$ . Seemingly insignificant, this error accumulates over the path, leading to a substantial mismatch in the gradients. When addressed in our **DiffGrad** module (by providing the accurate times), the **adjoint**-based attack becomes far more effective than previously thought (see §5).

Despite this approximation's accuracy when properly implemented, it is still sub-optimal and is not suitable for *discrete-time DBP*. Thus, adaptive attacks may benefit from an efficient implementation of *eq. (6)*. This can be achieved via checkpointing [9], which retains **only** intermediate outputs (e.g.,  $\hat{\boldsymbol{x}}(t)$  in *DBP*). In backpropagation, if we have the gradient  $\nabla_{\hat{\boldsymbol{x}}(t+dt)}$ , we can recompute  $\hat{\boldsymbol{x}}(t+dt)$  from  $\hat{\boldsymbol{x}}(t)$  to retrieve the dependencies and then use *eq. (6)* to recursively obtain  $\nabla_{\hat{\boldsymbol{x}}(t)}$ , overcoming memory limitations. Recently, Kang et al. [26] proposed checkpointing for *DBP*,

but their code only implements this technique for **DDPM**-based *DBP* (discrete), continuing to view the continuous setting as an integral for which they utilize the (erroneous) **adjoint** method. However, as implementations of the continuous view resort to discretization (see §2), we observe checkpointing is applicable to both paradigms. Liu et al. [33] also suggest checkpointing, reporting limited improvement over approximations. Their code has not been released. Yet, given **DiffGrad**'s superiority (see §5), their findings can be attributed to the factors listed below complicating accurate gradient calculation that we address:

1) *Eliminating Rounding Errors*: Rounding issues may emerge when implementing checkpointing over *torchsde* solvers: Given the starting time  $t^*$ , the solver internally converts it into a *PyTorch* tensor, iteratively calculating the intermediate outputs by adding negative time increments to this tensor. On the other hand, checkpointing requires re-calculating the intermediate steps' samples during backpropagation. If this code is oblivious to *torchsde*'s conversion of the initial time into a *PyTorch* tensor, it will continue to treat it as a floating point number, updating it with increments of the time step to obtain each intermediate  $t$  used to re-compute the dependencies. The *PyTorch* implementation does not aim for 100% accuracy, leading to minute discrepancies in the current value of  $t$  compared to pure floating-point operations. These inaccuracies accumulate over the time horizon, potentially severely affecting the gradients. Instead, we ensure both the solver and checkpointing code use the same objects (either floating points or tensors).

2) *Reproducing Stochasticity*: Calculating  $d\hat{\boldsymbol{x}}$  in *eq. (5)* involves randomness. Yet, vanilla checkpointing only stores the intermediate  $\hat{\boldsymbol{x}}(t)$ s. Hence,  $\hat{\boldsymbol{x}}(t+dt)$  will differ between the propagation phases as  $d\hat{\boldsymbol{x}}$  is computed via different random variables. We restructure the logic computing  $d\hat{\boldsymbol{x}}$ : We define a function *calc.dx* that accepts the noise as an external parameter and utilize a *Noise Sampler NS*, initialized upon every forward propagation. For each  $t$ , *NS* returns random noise to pass to *calc.dx*. Instead of  $\hat{\boldsymbol{x}}(0)$  only, forward propagation also outputs *NS* and a state *S* containing all  $\hat{\boldsymbol{x}}(t)$ s. These objects are used to restore the path in backpropagation. The memory cost is  $\mathcal{O}(\frac{t^*}{|dt|})$ , storing only *NS*, and all  $\hat{\boldsymbol{x}}(t)$ s, each with a negligible footprint ( $\mathcal{O}(1)$ ) compared to graph dependencies [26]. Liu et al. [33] do not discuss this challenge, suggesting it may be a reason behind their sub-optimal results. While Kang et al. [26] account for this component, they only apply checkpointing to *discrete-time DBP*. The paper also provides no results for the standard adaptive attack in this setting, evaluating only extensions that combine accurate gradients with additional methods. In §5, we challenge these enhancements' validity.

3) *Guidance Gradients*: *DBP* can employ additional *guidance* components in the reverse pass to retain key information, allowing for an increased budget  $t^*$  to better coun-

teract AEs [49]. As guidance is obtained by applying a function  $g\_fn$  to  $\hat{x}(t)$ , it creates paths from  $x$  to the loss that basic backpropagation fails to consider. We extend the process to include these “guidance” gradients. To our knowledge, we are the first to consider this component, potentially explaining the vast improvement over reported results [33]. As this is specific to guided schemes, we defer details to Supplemental B.1. Our gradient calculation pseudo-code is in Supplemental B.2 with a detailed analysis.

### 4.3. Defeating Increased Stochasticity

Despite the efficacy of correct gradients, *DBP*’s stochasticity boosts its robustness in the *MV* setting (see §3). Typical adversarial strategies incur high-frequency changes as they directly operate on pixels, potentially altering each significantly w.r.t. its neighbors. This leads to visual inconsistencies, limiting the distortion budget. Such modifications are also easily masked by *DBP*’s noise. Accounting for pixel correlations through systemic, low-frequency (*LF*) changes allows for larger perturbations and withstands randomness.

Thus, our *LF* method is inspired by a recent attack, namely *UnMarker* [27], on image watermarking that employs novel units termed *Optimizable Filters (OFs)*. In signal processing, a filter is a smoothing operation defined by a kernel  $\mathcal{K} \in \mathbb{R}^{M \times N}$  (with non-negative values that sum to 1), with which the input is convolved. The output at each pixel is a weighted average of all pixels in its  $M \times N$  vicinity, depending on the weights assigned by  $\mathcal{K}$ . Hence, filters incur systemic changes. Yet, they apply the same operation universally, unable to produce stealthy AEs, as the changes required to alter the label will be uniformly destructive. *UnMarker*’s *OFs* allow each pixel  $(i, j)$  to have its own kernel  $\mathcal{K}^{i,j}$  to customize the filtering at each point.  $\mathcal{K}^*$  is the set of all per-pixel  $\mathcal{K}^{i,j}$ s. The weights  $\theta_{\mathcal{K}^*}$  are learned via feedback from a perceptual metric (*lpips*) [65], leading to an assignment that ensures similarity while maximizing the destruction at visually non-critical regions to optimize a specific objective. Note that the *lpips* constraint replaces the traditional norm constraint. To guarantee similarity, they also impose geometric constraints via *color kernels*  $\sigma_c$ , similar to *guided* filters (details in Supplemental C.1).

We subject  $x$  to a chain  $\overset{\mathbb{B}}{O_F} \equiv O_{F\mathcal{K}_1^*, \omega, \sigma_{c_1}} \circ \dots \circ O_{F\mathcal{K}_B^*, \omega, \sigma_{c_B}}$  of *OFs* similar to *UnMarker*, replacing the objective pertaining to watermark removal in the learning process of the filters’ weights with the loss over  $\mathcal{M}$ . Each  $O_{F\mathcal{K}_b^*, \omega, \sigma_{c_b}}$  has a kernel set  $\mathcal{K}_b^*$  (with wights  $\theta_{\mathcal{K}_b^*}$  and shape  $M_b \times N_b$ ), and  $\sigma_{c_b}$ . The optimization problem is:

$$x_{adv} = \underset{\{\theta_{\mathcal{K}_b^*}, \delta\}}{\operatorname{argmin}} \left[ \begin{array}{c} \ell_G^{\mathcal{M}}(\overset{\mathbb{B}}{O_F}(x + \delta), y) \\ + c \cdot \max\{\mathit{lpips}(x, \overset{\mathbb{B}}{O_F}(x + \delta)) - \tau_p, 0\} \end{array} \right] \quad (7)$$

$\ell_G^{\mathcal{M}}$  denotes any loss as defined in §3.  $\delta$  is a modifier that directly optimizes  $x$ , similar to traditional attacks. AEs are generated by manipulating  $x$  via  $\delta$  and propagating the re-

sult through the filters. While direct modifications alone do not cause systemic changes, with *OFs*, they are smoothed over neighbors of the receiving pixels.  $\delta$  allows disruptions beyond interpolations. Similar to *UnMarker*, we chain several *OFs* with different shapes to explore various interpolations. Optimization is iterative (code in Supplemental C.3).  $\max\{\mathit{lpips}(x, \overset{\mathbb{B}}{O_F}(x + \delta)) - \tau_p, 0\}$  enforces similarity: If the distance exceeds  $\tau_p$ , the *lpips* gradients lower it in the next iteration. Otherwise, it returns 0, minimizing  $\ell_G^{\mathcal{M}}$  unconditionally. This gives a solution within the  $\tau_p$  constraint (violating outputs are discarded), yielding optimal  $\{\hat{\theta}_{\mathcal{K}_b^*}, \hat{\delta}\}$  s.t.  $x_{adv} = \overset{\mathbb{B}}{O_F}(x + \hat{\delta})$ , where  $\overset{\mathbb{B}}{O_F}$  are the filters with  $\{\hat{\theta}_{\mathcal{K}_b^*}\}$ .

## 5. Experiments

Here, we evaluate *DBP*, demonstrating its significantly degraded performance under non-bounded optimizations, and the unparalleled efficacy of our low-frequency method.

### 5.1. Experimental Setting

**Datasets.** We experiment with *CIFAR-10* [28] and *ImageNet* [14], using 256 random test samples for each due to *DBP*’s high costs. While several works [26, 31, 36] use 512 samples, this is prohibitive given our variety of threat models, attacks, and systems. Earlier work [56] that considers the costly *MV* setup uses fewer *ImageNet* samples (100).

**Models.** WideResNet-28-10 and WideResNet-70-16 [61] are used for *CIFAR-10*, and ResNet-50 [23], WideResNet-50-2, and DeiT-S [17] for *ImageNet*, similar to [26, 36]. For *VP-SDE DBP (DiffPure)* [36], the *DMs* [15, 45] are those from the original work. We also experiment with the *Guided-DDPM* (see §4.2), *GDMP* [49], due to its *SOTA* robustness, using the author-evaluated *DMs* [15, 25]. The settings match the original optimal setup [36, 49]: For *Diffpure*,  $t^* = 0.1$  for *CIFAR-10* and  $t^* = 0.15$  for *ImageNet*. For *GDMP*, a *CIFAR-10* sample is purified  $m = 4$  times, with each iteration running for 36 steps ( $t^* = 0.036$ ), using *MSE* guidance [49]. *ImageNet* uses 45 steps ( $m = 1$ ) under *DDPM*-acceleration [15] with *SSIM* guidance [50].

**Strategy.** To compare *DiffGrad* (the gradient module provided by our *DiffBreak* toolkit) with previous works [26, 31, 33, 36, 49], we use *AutoAttack*- $\ell_\infty$  [12] with  $\epsilon_\infty = 8/255$  for *CIFAR-10* and  $\epsilon_\infty = 4/255$  for *ImageNet*. For *LF* (see §4.3), we use *VGG-LIPIPS* [65] as the distance metric with  $\tau_p = 0.05$  as it guarantees imperceptibility [22, 27]. The remaining parameters are similar to *UnMarker*’s [27] (see Supplemental C.2). Optimizations run for 100 iterations, as in [26, 36]. The number of (*EoT*) samples  $N$  (see §4.1) is 128 for *CIFAR-10* and 16 for *ImageNet*.

**Metric.** We report the *robust accuracy* similar to previous work. Under *SP*, this is the portion of samples correctly labeled by the classifier and for which the attacker fails to even cause a **single** misclassification. For *MV*, this is the

portion of samples that, when propagated through multiple random paths, the majority of copies are labeled correctly.

**Baselines.** We focus on the works in Tables 1 & 2 that, to our knowledge, are the only papers proposing or evaluating unexplored optimization-based attacks (that do not require additional, often prohibitive resources [10, 13]) on *DBP* with advanced classifiers, differing in the gradient calculation methods. Due to memory limitations (see §4.2), *GDMP* is originally [49] evaluated with inferior attacks using the **blind** approach where gradients are obtained by directly feeding samples into the classifier ignoring *DBP*, and **BPDA**, which approximates the defense as the identity function during back-propagation [3]. For *DiffPure*, Nie et al. [36] suggested the **adjoint** method. Yet, its inability to impact the defense (because the flaws we uncover in §4.2 were not known) and unsuitability for **DDPM** urged Lee and Kim [31] to consider a **surrogate** approach to approximate the gradients, performing the reverse pass with fewer steps during backpropagation to reduce the memory overhead and using standard automatic differentiation to compute these approximate gradients. Liu et al. [33] and **DiffAttack** [26] use checkpointing for the full gradients but report sub-optimal results (see §4.2). **DiffAttack** also employs *per-step* losses along the reverse pass to interfere with the input’s reconstruction. Yet, as we showed the adaptive attack controls *DBP*’s outputs, this approach is of no added value when accurate gradients are available (see §5.2).

## 5.2. Revisiting Norm-Bounded Adversarial Attacks

Existing works focus on norm-bounded ( $l_\infty$  and  $l_2$ ) attacks in the *SP* setting. For *DBP*,  $l_\infty$  has repeatedly proven superior [26, 31, 33], making it the focus of our evaluations.

The results are in Tables 1 & 2. As no previous works evaluate *GDMP* for *ImageNet* under adaptive attacks, we perform the first such evaluation and also include WideResNet-70-16 for *CIFAR-10*. All works, including ours, use the official *DBP* code [36, 49], reporting similar clean accuracies (CI-Acc) in the absence of attacks, with minor variations due to the different sample sets. Thus, we can attribute robust accuracy (Rob-Acc) differences to the gradient methods, allowing us to perform comparisons with their numbers since we essentially perform the same experiment, and our **DiffGrad** only addresses backpropagation issues, challenging their specific findings (we verified on a control set that *DBP* exhibits similar robustness to that reported earlier without our modifications). Recall that our main goal is to show *DBP*’s inefficacy. The strongest previous attack on *DiffPure* is **DiffAttack**, which brings *CIFAR-10*’s best Rob-Acc to 45.31% and *ImageNet*’s to 31.25%. For *GDMP*, the best attack on *CIFAR-10*’s WideResNet-28-10 is the **surrogate**— 24.06% (other classifiers are not considered). For papers evaluating several methods, we chose their best. Lee and Kim [31] find their **surrogate**

Table 1. *SOTA* comparison using *AutoAttack*- $l_\infty$  on *CIFAR-10* ( $\epsilon_\infty=8/255$ ). † indicates strategy is *PGD*. Our results are in bold.

Models	Pur.	Gradient Method	CI-Acc %	Rob-Acc %
WideResNet-28-10	<i>DiffPure</i> [36]	<b>Adjoint</b> (Nie et al. [36])	89.02	70.64
		<b>DiffAttack</b> (Kang et al. [26])	89.02	46.88
		<b>Surrogate</b> (Lee and Kim [31])†	90.07	46.84
		<b>Full</b> (Liu et al. [33])	89.26	55.96
		<b>Full-DiffGrad</b> (Ours)	89.46	<b>8.59</b>
	<i>GDMP</i> [49]	<b>Blind</b> ( <i>GDMP</i> Wang et al. [49])	93.50	90.06
		<b>BPDA</b> (Lee and Kim [31])	89.96	75.59
		<b>Surrogate</b> (Lee and Kim [31])†	89.96	24.06
		<b>Full</b> (Liu et al. [33])	91.80	40.97
		<b>Full-DiffGrad</b> (Ours)	93.36	<b>6.25</b>
WideResNet-70-16	<i>DiffPure</i> [36]	<b>Adjoint</b> (Nie et al. [36])	90.07	71.29
		<b>DiffAttack</b> (Kang et al. [26])	90.07	45.31
		<b>Surrogate</b> (Lee and Kim [31])†	90.43	51.13
		<b>Adjoint-DiffGrad</b> (Ours)	89.06	<b>26.70</b>
		<b>Full-DiffGrad</b> (Ours)	89.06	<b>17.58</b>
	<i>GDMP</i> [49]	<b>Full-DiffGrad</b> (Ours)	92.58	<b>12.11</b>

Table 2. Comparison with the *SOTA* using *AutoAttack*- $l_\infty$  on *ImageNet* under *SP* ( $\epsilon_\infty = 4/255$ ). Our results are in bold.

Models	Pur.	Gradient Method	CI-Acc %	Rob-Acc %
WideResNet-50-2	<i>DiffPure</i> [36]	<b>Adjoint</b> (Nie et al. [36])	71.16	44.39
		<b>DiffAttack</b> (Kang et al. [26])	71.16	31.25
		<b>Full-DiffGrad</b> (Ours)	74.22	<b>12.11</b>
DeiT-S	<i>DiffPure</i> [36]	<b>Adjoint</b> (Nie et al. [36])	73.63	43.18
		<b>DiffAttack</b> (Kang et al. [26])	73.63	32.81
		<b>Adjoint-DiffGrad</b> (Ours)	74.22	<b>19.15</b>
		<b>Full-DiffGrad</b> (Ours)	74.22	<b>21.09</b>
	<i>GDMP</i> [49]	<b>Full-DiffGrad</b> (Ours)	69.14	<b>20.70</b>

integrates best with *PGD* [29]. As we did not observe the same with our method, we use *AutoAttack*.

Our findings are far superior: While the best results are obtained with the full gradients, the **adjoint** method provides highly accurate approximations [32]. Thus, we question the previous findings regarding its ineffectiveness, attributing them to the flaws identified in §4.2. Accordingly, we start by applying our proposed fixes to *torchsde*’s **adjoint** module and run *AutoAttack* on *ImageNet*’s DeiT-S and *CIFAR-10*’s WideResNet-70-16. The results— **Adjoint-DiffGrad** in Tables 1 & 2— show significant vulnerability of *DiffPure*, drastically outperforming previous work. We now implement our full gradient module that is also applicable to both *DBP* schemes, verifying it provides the exact gradients (see Supplemental D). Our attack’s— **Full-DiffGrad** in Tables 1 & 2— efficacy is unprecedented: For *DiffPure*, *CIFAR-10*’s Rob-Accs decline by at least 27.73%, reaching 8.59% while *ImageNet*’s best Rob-Acc becomes 21.09%. The numbers for *GDMP* similar. Our **Adjoint-DiffGrad** slightly outperforms **Full-DiffGrad** on DeiT-S due to different random paths. Yet, the latter has a clear advantage otherwise. In Supplemental E, we also re-evaluate **DiffAttack** with the full gradients, showing its *per-step* losses can be counterproductive. Our attack undermines *DBP*’s robustness under *SP*.

## 5.3. *DBP* Under a Stricter Threat Model

Despite the adaptive attack’s efficacy, we may still better exploit *DBP*’s stochasticity for robustness. As *DMs* restore

Table 3. Optimized  $AutoAttack-\ell_\infty$  under  $MV$  ( $\epsilon_\infty = 4/255$  for *ImageNet* and  $\epsilon_\infty = 8/255$  for *CIFAR-10*).

Pur.	Dataset	Models	Cl-Acc %	Rob-Acc %
DiffPure [36]	<i>ImageNet</i>	WideResNet-50-2	77.02	<b>29.69</b>
		DeiT-S	77.34	<b>32.81</b>
	<i>CIFAR-10</i>	WideResNet-70-16	92.19	<b>47.72</b>
		DeiT-S	75.00	<b>32.83</b>
GDMP [49]	<i>CIFAR-10</i>	WideResNet-28-10	93.36	<b>29.69</b>
		WideResNet-70-16	92.19	<b>32.81</b>

noisy inputs, *DBP*'s noise can dilute adversarial effects. While §5.2 shows these perturbations will likely affect the classifier through at least a single random path, the noise, when sufficiently large, may still mask them in the general case, preserving the correct label in expectation. Xiao et al. [56] proposed a *majority-vote* setting for certified robustness. While certifiable guarantees pertain to resistance under a strict  $\ell_2$  budget, *AEs* can be visually identical to the benign inputs despite exceeding  $\ell_2$  limitations (e.g., *AutoAttack-\ell\_\infty*, *StAdv* [54]). Works on certified robustness via *DBP* [6, 7, 53, 56, 64] also fail to consider adaptive attacks that defy theoretical guarantees. Thus, we evaluate  $MV$ 's practical benefits. We test  $AutoAttack-\ell_\infty$  using our superior **Full-DiffGrad** gradient module and all classifiers from §5.2 except WideResNet-28-10 for *DiffPure* as its performance was shown far worse than WideResNet-70-16. Yet, we consider it for *GDMP* due to its prevalence in relevant works.

$MV$  requires a number of copies over which the majority vote is taken. We select it as the maximum batch size that fits into the *GPU* during a single run<sup>2</sup> (128 for *CIFAR-10* and 8 for *ImageNet*). Unlike *SP*, where attacks terminate after a single misclassification,  $MV$  requires many more iterations. These batch sizes are already computationally exhaustive, causing a single sample to occupy the entire *GPU* for 2–3 hours (upon failure to converge). Hence, larger numbers are infeasible. We are the first to combine  $MV$  with adaptive attacks, making our setup far more costly. We still verified on a small set the robustness gained by increasing the batch size from 32 to 128 for *CIFAR-10* is negligible, concluding Rob-Acc saturates at this number. Similarly, a batch size of 16 provides almost no improvement over 8 for *ImageNet*, and we chose the latter for practicality.

Table 3 demonstrates  $MV$ 's advantage: The worst Rob-Acc for *ImageNet* with *Diffpure* is 29.69%, compared to 12.11% under *SP*, while *CIFAR-10*'s WideResNet-70-16's Rob-Acc increases to 47.72% (+30.14%). For *GDMP*, *ImageNet*'s Rob-Acc rises to 32.83% (+12.13%) and *CIFAR-10*'s worst Rob-Acc becomes 29.69% (+23.44%). We advise future works to focus on  $MV$  as it improves robustness despite its costs. Yet, *DBP* remains currently broken by a previously unexplored class of *AEs*, as we show next.

<sup>2</sup>All experiments were conducted on a 40GB NVIDIA A100 GPU.

Table 4. Performance of  $LF$  attack under  $MV$ .

Pur.	Dataset	Models	Cl-Acc %	Rob-Acc %
DiffPure [36]	<i>ImageNet</i>	ResNet-50	72.54	<b>0.00</b>
		WideResNet-50-2	77.02	<b>0.00</b>
		DeiT-S	77.34	<b>0.00</b>
	<i>CIFAR-10</i>	WideResNet-28-10	92.19	<b>2.73</b>
		WideResNet-70-16	92.19	<b>3.13</b>
		ResNet-50	73.05	<b>0.39</b>
GDMP [49]	<i>ImageNet</i>	WideResNet-50-2	71.88	<b>0.00</b>
		DeiT-S	75.00	<b>0.39</b>
		WideResNet-28-10	93.36	<b>0.00</b>
	<i>CIFAR-10</i>	WideResNet-70-16	92.19	<b>0.39</b>

#### 5.4. *DBP* Against Low-Frequency *AEs*

Our final question is: Can *DBP*'s performance be degraded further under  $MV$ ? Based on our analysis in §4.3, this is possible with our  $LF$  strategy. The results for  $LF$  (which uses our **Full-DiffGrad** backbone for backpropagation) are in Table 4. We also include a ResNet-50 classifier for *ImageNet* to better support our claims.  $LF$ 's success is unprecedented: not only does it defeat all classifiers completely, leaving the strongest with Rob-Acc of 3.13%, but it also does so in the challenging  $MV$  setting, where previous approaches will suffer performance degradation compared to the results reported in §5.2, similar to what we showed for *AutoAttack* with our superior **DiffGrad** gradient module.

**Discussion & Future Work.** Our attack's stealthiness is guaranteed due to the *lpips* metric with a threshold proven to ensure this behavior [22, 27]. We provide sample images in Supplemental F and also include samples for the known *StAdv* [54], showing it fails to generate stealthy perturbations on *DBP*. Our findings highlight a shortcoming of the current methodology for evaluating robustness as the focus on norm-based attacks overshadows other techniques that are critical in today's landscape, where low-frequency attacks pose threats to which the community has not yet developed responses. We recommend investing efforts in developing mitigations against this class in future works.

## 6. Conclusion

We scrutinized *DBP*'s theory, nullifying core assumptions. Accordingly, we investigated previous findings, attributing them to implementation flaws, and proposed fixes to enable reliable evaluations, exposing degraded performance under adaptive attacks. Finally, we evaluated *DBP* in a stricter setup, wherein we found its increased stochasticity leaves it partially immune to norm-bounded *AEs*. Yet, our novel low-frequency approach defeats this defense in both settings. We find current *DBP* is not a viable response to *AEs*, highlighting the need for improvements.

**Acknowledgments.** This work was supported by the NSERC Discovery Grant RGPIN-2020-04722 and the Waterloo-Huawei Joint Innovation Laboratory.



## References

- [1] Amazon Web Services (AWS). <https://aws.amazon.com>. 3
- [2] Brian DO Anderson. Reverse-time diffusion equation models. *Stochastic Processes and their Applications*, 1982. 3
- [3] Anish Athalye, Nicholas Carlini, and David Wagner. Obfuscated gradients give a false sense of security: Circumventing defenses to adversarial examples. In *International conference on machine learning*, 2018. 1, 2, 7
- [4] Jacob Buckman, Aurko Roy, Colin Raffel, and Ian J. Goodfellow. Thermometer encoding: One hot way to resist adversarial examples. In *6th International Conference on Learning Representations, ICLR*, 2018. 1
- [5] Nicholas Carlini and David Wagner. Towards evaluating the robustness of neural networks. In *2017 IEEE Symposium on Security and Privacy (SP)*, 2017. 15, 16
- [6] Nicholas Carlini, Florian Tramer, Krishnamurthy Dvijotham, Leslie Rice, Mingjie Sun, and J Zico Kolter. (certified!!) adversarial robustness for free! In *The Eleventh International Conference on Learning Representations*, 2023. 1, 3, 8
- [7] Huanran Chen, Yinpeng Dong, Shitong Shao, Zhongkai Hao, Xiao Yang, Hang Su, and Jun Zhu. Your diffusion model is secretly a certifiably robust classifier. *CoRR*, 2024. 3, 8
- [8] Huanran Chen, Yinpeng Dong, Zhengyi Wang, Xiao Yang, Chengqi Duan, Hang Su, and Jun Zhu. Robust classification via a single diffusion model, 2024. 1, 3
- [9] Tianqi Chen, Bing Xu, Chiyuan Zhang, and Carlos Guestrin. Training deep nets with sublinear memory cost. *arXiv preprint arXiv:1604.06174*, 2016. 2, 5
- [10] Xinquan Chen, Xitong Gao, Juanjuan Zhao, Kejiang Ye, and Cheng-Zhong Xu. Advdiffuser: Natural adversarial example synthesis with diffusion models. In *IEEE/CVF International Conference on Computer Vision, ICCV*, 2023. 7
- [11] Jeremy Cohen, Elan Rosenfeld, and J. Zico Kolter. Certified adversarial robustness via randomized smoothing. In *Proceedings of the 36th International Conference on Machine Learning, ICML*, 2019. 1
- [12] Francesco Croce and Matthias Hein. Reliable evaluation of adversarial robustness with an ensemble of diverse parameter-free attacks. In *International conference on machine learning*, 2020. 2, 6
- [13] Xuelong Dai, Kaisheng Liang, and Bin Xiao. Advdiff: Generating unrestricted adversarial examples using diffusion models. In *Computer Vision - ECCV*, 2024. 7
- [14] Jia Deng, Wei Dong, Richard Socher, Li-Jia Li, Kai Li, and Li Fei-Fei. ImageNet: A large-scale hierarchical image database. In *2009 IEEE conference on computer vision and pattern recognition*, 2009. 6
- [15] Prafulla Dhariwal and Alexander Quinn Nichol. Diffusion models beat gans on image synthesis. In *Advances in Neural Information Processing Systems 34: Annual Conference on Neural Information Processing Systems, NeurIPS*, 2021. 1, 6
- [16] Guneet S. Dhillon, Kamyar Azizzadenesheli, Zachary C. Lipton, Jeremy Bernstein, Jean Kossaifi, Aran Khanna, and Animashree Anandkumar. Stochastic activation pruning for robust adversarial defense. In *6th International Conference on Learning Representations, ICLR*, 2018. 1
- [17] Alexey Dosovitskiy, Lucas Beyer, Alexander Kolesnikov, Dirk Weissenborn, Xiaohua Zhai, Thomas Unterthiner, Mostafa Dehghani, Matthias Minderer, Georg Heigold, Sylvain Gelly, Jakob Uszkoreit, and Neil Houlsby. An image is worth 16x16 words: Transformers for image recognition at scale. In *9th International Conference on Learning Representations, ICLR*, 2021. 6
- [18] Yue Gao, Iliia Shumailov, Kassem Fawaz, and Nicolas Papernot. On the limitations of stochastic pre-processing defenses. In *Advances in Neural Information Processing Systems 35: Annual Conference on Neural Information Processing Systems, NeurIPS*, 2022. 1
- [19] Ian Goodfellow, Jean Pouget-Abadie, Mehdi Mirza, Bing Xu, David Warde-Farley, Sherjil Ozair, Aaron Courville, and Yoshua Bengio. Generative adversarial nets. *Advances in neural information processing systems*, 2014. 1
- [20] Ian J. Goodfellow, Jonathon Shlens, and Christian Szegedy. Explaining and harnessing adversarial examples. In *3rd International Conference on Learning Representations, ICLR*, 2015. 1
- [21] Chuan Guo, Mayank Rana, Moustapha Cissé, and Laurens van der Maaten. Countering adversarial images using input transformations. In *6th International Conference on Learning Representations, ICLR*, 2018. 1
- [22] Qingying Hao, Licheng Luo, Steve TK Jan, and Gang Wang. It's not what it looks like: Manipulating perceptual hashing based applications. In *Proceedings of the 2021 ACM SIGSAC Conference on Computer and Communications Security*, 2021. 6, 8
- [23] Kaiming He, Xiangyu Zhang, Shaoqing Ren, and Jian Sun. Deep residual learning for image recognition. In *Proceedings of the IEEE conference on computer vision and pattern recognition*, 2016. 6
- [24] Mitch Hill, Jonathan Craig Mitchell, and Song-Chun Zhu. Stochastic security: Adversarial defense using long-run dynamics of energy-based models. In *9th International Conference on Learning Representations, ICLR*, 2021. 1
- [25] Jonathan Ho, Ajay Jain, and Pieter Abbeel. Denoising diffusion probabilistic models. *Advances in neural information processing systems*, 2020. 3, 6, 12
- [26] Mintong Kang, Dawn Song, and Bo Li. Diffattack: Evasion attacks against diffusion-based adversarial purification. *Advances in Neural Information Processing Systems*, 2024. 2, 3, 4, 5, 6, 7, 17
- [27] Andre Kassis and Urs Hengartner. UnMarker: A Universal Attack on Defensive Image Watermarking . In *2025 IEEE Symposium on Security and Privacy (SP)*, 2025. 2, 6, 8, 15, 25
- [28] Alex Krizhevsky, Geoffrey Hinton, et al. Learning multiple layers of features from tiny images. 2009. 6
- [29] Alexey Kurakin, Ian J. Goodfellow, and Samy Bengio. Adversarial examples in the physical world. In *Artificial intelligence safety and security*. Chapman and Hall/CRC, 2018. 7

- [30] Yann LeCun, Sumit Chopra, Raia Hadsell, M Ranzato, Fujie Huang, et al. A tutorial on energy-based learning. *Predicting structured data*, 2006. 1
- [31] Minjong Lee and Dongwoo Kim. Robust evaluation of diffusion-based adversarial purification. In *Proceedings of the IEEE/CVF International Conference on Computer Vision*, 2023. 2, 3, 4, 6, 7
- [32] Xuechen Li, Ting-Kam Leonard Wong, Ricky TQ Chen, and David Duvenaud. Scalable gradients for stochastic differential equations. In *International Conference on Artificial Intelligence and Statistics*, 2020. 2, 5, 7
- [33] Yiming Liu, Kezhao Liu, Yao Xiao, Ziyi Dong, Xiaogang Xu, Pengxu Wei, and Liang Lin. Towards better adversarial purification via adversarial denoising diffusion training. *CoRR*, 2024. 2, 3, 4, 5, 6, 7
- [34] Aleksander Madry, Aleksandar Makelov, Ludwig Schmidt, Dimitris Tsipras, and Adrian Vladu. Towards deep learning models resistant to adversarial attacks. In *6th International Conference on Learning Representations, ICLR*, 2018. 1
- [35] Dongyu Meng and Hao Chen. MagNet: a two-pronged defense against adversarial examples. In *ACM SIGSAC Conference on Computer and Communications Security*, 2017. 3
- [36] Weili Nie, Brandon Guo, Yujia Huang, Chaowei Xiao, Arash Vahdat, and Animashree Anandkumar. Diffusion models for adversarial purification. In *International Conference on Machine Learning, ICML*, 2022. 1, 2, 3, 4, 6, 7, 8, 18
- [37] Yidong Ouyang, Liyan Xie, and Guang Cheng. Improving adversarial robustness through the contrastive-guided diffusion process. In *Proceedings of the 40th International Conference on Machine Learning*, 2023. 1, 3
- [38] Tianyu Pang, Kun Xu, and Jun Zhu. Mixup inference: Better exploiting mixup to defend adversarial attacks. In *International Conference on Learning Representations*, 2019. 1, 3
- [39] Nicolas Papernot, Patrick McDaniel, Xi Wu, Somesh Jha, and Ananthram Swami. Distillation as a defense to adversarial perturbations against deep neural networks. In *IEEE Symposium on Security and Privacy*, 2016. 3
- [40] Rafael Pinot, Raphael Ettetdgui, Geovani Rizk, Yann Chevaleyre, and Jamal Atif. Randomization matters how to defend against strong adversarial attacks. In *Proceedings of the 37th International Conference on Machine Learning, ICML*, 2020. 1
- [41] Pouya Samangouei, Maya Kabkab, and Rama Chellappa. Defense-GAN: Protecting classifiers against adversarial attacks using generative models. In *International Conference on Learning Representations*, 2018. 1
- [42] Shawn Shan, Wenxin Ding, Emily Wenger, Haitao Zheng, and Ben Y Zhao. Post-breach recovery: Protection against white-box adversarial examples for leaked dnn models. In *Proceedings of the 2022 ACM SIGSAC Conference on Computer and Communications Security*, 2022. 3
- [43] Jascha Sohl-Dickstein, Eric Weiss, Niru Maheswaranathan, and Surya Ganguli. Deep unsupervised learning using nonequilibrium thermodynamics. In *International conference on machine learning*, 2015. 1, 2, 3, 12
- [44] Yang Song, Taesup Kim, Sebastian Nowozin, Stefano Ermon, and Nate Kushman. Pixeldefend: Leveraging generative models to understand and defend against adversarial examples. In *6th International Conference on Learning Representations, ICLR*, 2018. 1
- [45] Yang Song, Jascha Sohl-Dickstein, Diederik P. Kingma, Abhishek Kumar, Stefano Ermon, and Ben Poole. Score-based generative modeling through stochastic differential equations. In *9th International Conference on Learning Representations, ICLR*, 2021. 1, 2, 3, 5, 6, 12
- [46] Christian Szegedy, Wojciech Zaremba, Ilya Sutskever, Joan Bruna, Dumitru Erhan, Ian J. Goodfellow, and Rob Fergus. Intriguing properties of neural networks. In *2nd International Conference on Learning Representations, ICLR*, 2014. 1
- [47] Florian Tramèr, Nicholas Carlini, Wieland Brendel, and Aleksander Madry. On adaptive attacks to adversarial example defenses. In *Advances in Neural Information Processing Systems 33: Annual Conference on Neural Information Processing Systems 2020, NeurIPS 2020, December 6-12, 2020, virtual*, 2020. 1
- [48] Arash Vahdat, Karsten Kreis, and Jan Kautz. Score-based generative modeling in latent space. In *Advances in Neural Information Processing Systems 34: Annual Conference on Neural Information Processing Systems, NeurIPS*, 2021. 1
- [49] Jinyi Wang, Zhaoyang Lyu, Dahua Lin, Bo Dai, and Hongfei Fu. Guided diffusion model for adversarial purification. *arXiv preprint arXiv:2205.14969*, 2022. 1, 2, 3, 4, 6, 7, 8, 12
- [50] Zhou Wang, Alan C Bovik, Hamid R Sheikh, and Eero P Simoncelli. Image quality assessment: from error visibility to structural similarity. *IEEE transactions on image processing*, 2004. 6
- [51] Zekai Wang, Tianyu Pang, Chao Du, Min Lin, Weiwei Liu, and Shuicheng Yan. Better diffusion models further improve adversarial training. In *International Conference on Machine Learning, ICML*, 2023. 1
- [52] Eric Wong, Leslie Rice, and J. Zico Kolter. Fast is better than free: Revisiting adversarial training. In *8th International Conference on Learning Representations, ICLR*, 2020. 1
- [53] Quanlin Wu, Hang Ye, and Yuntian Gu. Guided diffusion model for adversarial purification from random noise. *CoRR*, 2022. 1, 3, 8
- [54] Chaowei Xiao, Jun-Yan Zhu, Bo Li, Warren He, Mingyan Liu, and Dawn Song. Spatially transformed adversarial examples. In *6th International Conference on Learning Representations, ICLR*, 2018. 8, 18, 25
- [55] Chang Xiao, Peilin Zhong, and Changxi Zheng. Enhancing adversarial defense by k-winners-take-all. In *International Conference on Learning Representations*, 2020. 1
- [56] Chaowei Xiao, Zhongzhu Chen, Kun Jin, Jiong Xiao Wang, Weili Nie, Mingyan Liu, Anima Anandkumar, Bo Li, and Dawn Song. Densepure: Understanding diffusion models towards adversarial robustness. In *Workshop on Trustworthy and Socially Responsible Machine Learning, NeurIPS 2022*, 2022. 1, 2, 3, 6, 8

- [57] Cihang Xie, Jianyu Wang, Zhishuai Zhang, Zhou Ren, and Alan Yuille. Mitigating adversarial effects through randomization. In *International Conference on Learning Representations*, 2018. [1](#)
- [58] Yuzhe Yang, Guo Zhang, Dina Katabi, and Zhi Xu. Me-net: Towards effective adversarial robustness with matrix estimation. In *International Conference on Machine Learning*, 2019. [1](#)
- [59] Cheng-Han Yeh, Kuanchun Yu, and Chun-Shien Lu. Test-time adversarial defense with opposite adversarial path and high attack time cost. *arXiv preprint arXiv:2410.16805*, 2024. [3](#)
- [60] Jongmin Yoon, Sung Ju Hwang, and Juho Lee. Adversarial purification with score-based generative models. In *International Conference on Machine Learning*, 2021. [3](#)
- [61] Sergey Zagoruyko. Wide residual networks. *arXiv preprint arXiv:1605.07146*, 2016. [6](#)
- [62] Boya Zhang, Weijian Luo, and Zhihua Zhang. Purify++: Improving diffusion-purification with advanced diffusion models and control of randomness. *CoRR*, 2023. [1](#), [3](#)
- [63] Hongyang Zhang, Yaodong Yu, Jiantao Jiao, Eric P. Xing, Laurent El Ghaoui, and Michael I. Jordan. Theoretically principled trade-off between robustness and accuracy. In *Proceedings of the 36th International Conference on Machine Learning, ICML*, 2019. [1](#)
- [64] Jiawei Zhang, Zhongzhu Chen, Huan Zhang, Chaowei Xiao, and Bo Li. DiffSmooth: Certifiably robust learning via diffusion models and local smoothing. In *32nd USENIX Security Symposium (USENIX Security 23)*, 2023. [1](#), [2](#), [3](#), [8](#)
- [65] Richard Zhang, Phillip Isola, Alexei A Efros, Eli Shechtman, and Oliver Wang. The unreasonable effectiveness of deep features as a perceptual metric. In *CVPR*, 2018. [6](#), [15](#)

# Unlocking The Potential of Adaptive Attacks on Diffusion-Based Purification

## Supplementary Material

### A. Equivalence of DDPM and VP-SDE

An alternative to the *continuous-time* view described in §2 (i.e., **VP-SDE**) is *Denoising diffusion probabilistic modeling* (**DDPM**) [25, 43], which considers a *discrete-time* framework (*DM*) where the forward and reverse passes are characterized by a maximum number of steps  $T$ . Here, the forward pass is a Markov chain:

$$\mathbf{x}_i = \sqrt{1 - \beta_i} \mathbf{x}_{i-1} + \sqrt{\beta_i} \mathbf{z}_i$$

where  $\mathbf{z}_i \sim \mathcal{N}(\mathbf{0}, \mathbf{I}_d)$  and  $\beta_i$  is a small positive noise scheduling constant. Defining  $dt = \frac{1}{T}$ , we know due to Song et al. [45] that when  $T \rightarrow \infty$  (i.e.,  $dt \rightarrow 0$ , which is the effective case of interest), this converges to the *SDE* in eq. (1) (with the drift and diffusion function  $\mathbf{f}$  and  $g$  described in §2). The reverse pass is also a Markov chain given as:

$$d\hat{\mathbf{x}} = \hat{\mathbf{x}}_{i-1} - \hat{\mathbf{x}}_i = \frac{1}{\sqrt{1 - \beta_i}} ((1 - \sqrt{1 - \beta_i}) \hat{\mathbf{x}}_i + \beta_i \mathbf{s}_\theta(\hat{\mathbf{x}}_i, i)) + \sqrt{\beta_i} \mathbf{z}_i \quad (\text{S1})$$

When  $T \rightarrow \infty$ ,  $d\hat{\mathbf{x}}$  converges to eq. (4) (see [45]). Thus, the two views are effectively equivalent. Accordingly, we focus on the continuous view, which encompasses both frameworks. For discrete time,  $\mathbf{x}(t)$  will be used to denote  $\mathbf{x}_{\lfloor \frac{t}{dt} \rfloor}$ .

### B. Details on Our DiffGrad Gradient Module

#### B.1. Accounting for The Guidance Gradients

In schemes that involve guidance, it is typically obtained by applying a function  $\mathbf{g\_fn}$  to  $\hat{\mathbf{x}}(t)$  at each step. For instance, in *Guided-DDPM* [49], the original sample  $\mathbf{x}$  is used to influence the reverse procedure to retain key semantic information, allowing for an increased budget  $t^*$  to better counteract adversarial perturbations. Effectively, it modifies eq. (S1) describing the reverse pass of **DDPM** as:

$$d\hat{\mathbf{x}} = \frac{1}{\sqrt{1 - \beta_i}} ((1 - \sqrt{1 - \beta_i}) \hat{\mathbf{x}}_i + \beta_i \mathbf{s}_\theta(\hat{\mathbf{x}}_i, i)) - s \beta_i \nabla_{\hat{\mathbf{x}}_i} \mathbf{GC}(\hat{\mathbf{x}}_i, \mathbf{x}) + \sqrt{\beta_i} \mathbf{z}_i$$

where  $\mathbf{GC}$  is a guidance condition (typically a distance metric), each step minimizes by moving in the opposite direction of its gradient, while the scale  $s$  controls the guidance’s influence.

That is, in the specific case of *Guided-DDPM*,  $\mathbf{g\_fn}(\hat{\mathbf{x}}(t)) \equiv -\nabla_{\hat{\mathbf{x}}(t)} \mathbf{GC}(\hat{\mathbf{x}}(t), \mathbf{x})$ , where  $\mathbf{GC}$  is a distance metric. Nonetheless, other choices for  $\mathbf{g\_fn}$  may be employed in general. Typically, as the goal of the guidance is to ensure key information from the original sample  $\mathbf{x}$  is retained,  $\mathbf{g\_fn}$  will also *directly* involve this  $\mathbf{x}$  in addition to  $\hat{\mathbf{x}}(t)$  (e.g.,  $\mathbf{GC}$  above). Yet, a naive implementation would back-propagate the gradients to  $\mathbf{x}$  by only considering the path through  $\hat{\mathbf{x}}(t)$ . Yet, when  $\mathbf{g\_fn}$  relies on a *guide* constructed from  $\mathbf{x}$  to influence  $\hat{\mathbf{x}}(t)$  (e.g.,  $\mathbf{guide} \equiv \mathbf{x}$  in *Guided-DDPM*, it creates additional paths from  $\mathbf{x}$  to the loss through this *guide* at each step  $t$ . Accordingly, **DiffGrad** augments the process to include the gradients due to these paths. In the general case, this *guide* may not be identical to  $\mathbf{x}$  but can rather be computed based on  $\mathbf{x}$  or even completely independent (in which case no guidance gradients are collected). **DiffGrad** captures this nuance through an abstract function  $\mathbf{g\_aux}$  that, given  $\mathbf{x}$ , outputs the *guide*. Similar to eq. (6), we have that for each  $t$ , the gradient of any function  $F$  applied to  $\hat{\mathbf{x}}(0)$  w.r.t. *guide* due to the path from  $\hat{\mathbf{x}}(t + dt)$  to  $\hat{\mathbf{x}}(0)$  is given by:

$$\nabla_{\mathbf{guide}}^t F = \nabla_{\mathbf{guide}} \langle \hat{\mathbf{x}}(t + dt), \nabla_{\hat{\mathbf{x}}(t+dt)} F \rangle \quad (\text{S2})$$

as  $\hat{\mathbf{x}}(t + dt)$  is a function of *guide*. Recall that we are interested in  $F$ , which is the loss function over the classifier’s output on  $\hat{\mathbf{x}}(0)$ . The gradient of  $F$  w.r.t. *guide* is a superposition of all these paths’ gradients, given as:

$$\nabla_{\mathbf{guide}} F = \sum_t \nabla_{\mathbf{guide}}^t F \quad (\text{S3})$$

By the chain rule,  $F$ ’s gradient w.r.t  $\mathbf{x}$  due to the guidance paths, which we denote as  $\nabla_{\mathbf{x}}^g F$ , is:

$$\nabla_{\mathbf{x}}^g F = \nabla_{\mathbf{x}} \langle \mathbf{guide}, \nabla_{\mathbf{guide}} F \rangle \quad (\text{S4})$$

As a convention, for an unguided process or when *guide* and  $x$  are not related, we define the gradient returned from eq. (S4) as  $\nabla_x^g F \equiv \mathbf{0}$ , preserving correctness in general. Since  $x$  in this guided scenario traverses both the guidance and standard purification paths, the final gradient is the sum of both components.

Finally, automatic differentiation engines, by default, generate gradients without retaining dependencies on the inputs that produced them. Thus, when the guidance itself is in the form of a gradient as in the case of *Guided-DDPM* or other potential alternatives, its effects will not be back-propagated to  $x$  through any of the two paths described above, despite our proposed extensions. **DiffGrad** alters this behavior, retaining the dependencies of such gradient-based guidance metrics as well.

## B.2. Pseudo-Code for Our Memory-Efficient Gradient-Enabled Purification with DiffGrad

**DiffGrad**'s forward propagation logic is in Algorithm 1. The code in blue is optional, pertaining to the use of guidance. We highlight in red the portions that differ from standard forward propagation. First, we generate the guidance *guide* from  $x$  (line 1) and disable all graph dependency storage (line 2), enabling our code to run efficiently without attempting to store graphs that will lead to memory failures. Afterward (lines 3-5), we initialize  $S$  as an empty list and draw a random seed that is then used to invoke the abstract function *init\_noise\_sampler*, which returns a noise sampler that provides a reproducible random path for the backpropagation phase (see §4.2). After the input is diffused (lines 6-8) via eq. (2), lines 9-15 correspond to the reverse pass: At each step  $t$  (effectively  $i$ ),  $\hat{x}$  (that now represents  $\hat{x}(t)$ ) is first appended to  $S$ , which will eventually contain all such intermediate outputs (line 10). The noise provided by  $NS$  for the current step  $i$  is then retrieved (line 11) and used to compute  $d\hat{x}$  (line 12).  $d\hat{x}$  is then added to  $\hat{x}$  so that its current value becomes  $\hat{x}(t + dt)$ . This repeats until  $\hat{x} = \hat{x}(0)$ . Unlike the naive implementation, we only store the intermediate results. For efficiency, we also avoid saving the random noise for each step  $i$ , but utilize  $NS$  to reproduce those variables on demand. Before termination, we re-enable dependency storage (line 16) to ensure our code does not interfere with the execution of any other modules. Finally,  $\hat{x}(0)$  is returned together with the state  $S$  and the sampler  $NS$  that are stored internally for reproducibility during backpropagation.

---

**Algorithm 1:** Differentiable Purification with **DiffGrad**— Forward Propagation

---

```

Input: Sample  $x$ , Score model  $s_\theta$ , Optimal diffusion time  $t^*$ , step size  $dt$ , Noise scheduler  $\beta$ ,
Reverse diffusion function calc_dx, Noise sampler initializer init_noise_sampler
Guidance condition g_fn, Guidance scale  $s$ , Auxiliary guidance extractor g_aux
1  $steps \leftarrow \lfloor \frac{t^*}{dt} \rfloor$ , guide  $\leftarrow$  g_aux( $x$ ); /* Calc. #steps and init. guide */
2 disable_dependencies(); /* Dependencies enabled during forward
prop. Disable them. */
3  $S \leftarrow []$ ; /* Saved state (will eventually hold all
intermediate reverse steps' outputs) */
4  $seed \leftarrow$  random_seed(); /* Seed to initialize noise path */
5  $NS \leftarrow$  init_noise_sampler( $seed$ ); /* Reproducible sampler. */
6  $\alpha \leftarrow$  calc_alpha( $\beta$ ); /* Calc.  $\alpha$  factors from eq. (2) */
7 Draw  $\epsilon \sim \mathcal{N}(\mathbf{0}, I_d)$ ;
8  $\hat{x} \leftarrow \sqrt{\alpha(t^*)}x + \sqrt{1 - \alpha(t^*)}\epsilon$ ; /* Diffuse according to eq. (2) */
9 for  $i$  in  $steps, steps - 1, \dots, 1$  do
10 | S.append( $\hat{x}$ ); /* Set  $S[i] = \hat{x}(t)$  */
11 | step_noise  $\leftarrow$  NS.sample( $i$ ); /* Sample the random noise used to
calculate  $d\hat{x}$  at step  $i$  */
12 |  $d\hat{x} \leftarrow$  calc_dx( $\hat{x}$ ,  $s_\theta, i$ ,  $dt$ ,  $\beta$ , \
13 | step_noise, g_fn,  $s$ , guide); /* Calc.  $d\hat{x}$  according to
eq. (4) */
14 |  $\hat{x} \leftarrow \hat{x} + d\hat{x}$ ; /* Update  $\hat{x} = \hat{x}(t + dt)$  */
15 end
16 enable_dependencies(); /* Re-enable dependencies */
17 return  $\hat{x}$ ,  $S$ ,  $NS$ , guide

```

---

**DiffGrad**'s backpropagation logic is in Algorithm 2. Similar to earlier, red text refers to operations that deviate from traditional backpropagation, while blue lines are optional (guidance-related). In addition to the usual gradient  $\mathbf{grad}$  w.r.t.  $\hat{\mathbf{x}}(0)$ , the inputs include multiple parameters normally exclusive to forward propagation, as they are required to re-calculate the dependencies. Additionally, the algorithm accepts the saved state  $\mathcal{S}$ , and the same noise sampler  $\mathcal{NS}$  to retrieve the stochastic path of the forward propagation. Before providing details, we note that by definition  $\forall \mathbf{A}, \mathbf{B} \in \mathbb{R}^d$ , it holds that:

$$\langle \mathbf{A}, \mathbf{B} \rangle = \sum_d \mathbf{A} \odot \mathbf{B}$$

where  $\odot$  denotes the element-wise product. Therefore, in order to calculate the gradients w.r.t.  $\hat{\mathbf{x}}(t)$  and  $\mathbf{guide}$  as described in eq. (6) and eq. (S2), we may define an objective at each step  $t$  as:

$$Obj_t = \sum_d (\hat{\mathbf{x}}(t + dt) \odot \nabla_{\hat{\mathbf{x}}(t+dt)} F) \quad (S5)$$

and take its gradient w.r.t. the two elements of interest above, which explains the steps in our pseudo-code in Algorithm 2.

---

**Algorithm 2:** Differentiable Purification with **DiffGrad**— Backpropagation

---

**Input:** Loss gradient  $\mathbf{grad}$  w.r.t  $\hat{\mathbf{x}}_0$ , **Sample  $\mathbf{x}$** , **Score model  $s_\theta$** , **Optimal diffusion time  $t^*$** , **step size  $dt$** , **Noise scheduler  $\beta$** , **Reverse diffusion function  $\mathit{calc\_dx}$** , **State  $\mathcal{S} = \{\hat{\mathbf{x}}(dt * i) | i \in \llbracket \frac{t^*}{dt} \rrbracket\}$** , **Noise sampler  $\mathcal{NS}$**   
**Auxiliary guidance input  $\mathbf{guide}$** , **Guidance function  $\mathit{g\_fn}$** , **Guidance scale  $s$**

```

1  $\mathit{steps} \leftarrow \lfloor \frac{t^*}{dt} \rfloor$ ;
2  $\mathbf{g\_grad} \leftarrow \mathbf{0}$ ; /* Init. gradient w.r.t. guide */
3 for  $i$  in  $1, 2, \dots, \mathit{steps}$  do
4    $\hat{\mathbf{x}} \leftarrow \mathcal{S}[i]$ ; /* Set  $\hat{\mathbf{x}} = \hat{\mathbf{x}}(t)$  */
5    $\mathit{step\_noise} \leftarrow \mathcal{NS.sample}(i)$ ; /* Retrieve noise for step  $i$  */
6    $\mathit{enable\_dependencies}()$ ;
7    $d\hat{\mathbf{x}} \leftarrow \mathit{calc\_dx}(\hat{\mathbf{x}}, s_\theta, i, dt, \beta, \backslash$ 
8      $\mathit{step\_noise}, \mathit{g\_fn}, s, \mathbf{guide})$ ; /*  $\hat{\mathbf{x}}_{+dt} = \hat{\mathbf{x}}(t + dt)$  */
9    $\hat{\mathbf{x}}_{+dt} \leftarrow \hat{\mathbf{x}} + d\hat{\mathbf{x}}$ ; /*  $\hat{\mathbf{x}}_{+dt} = \hat{\mathbf{x}}(t + dt)$  */
10   $Obj_t \leftarrow \sum (\hat{\mathbf{x}}_{+dt} \odot \mathbf{grad})$ ; /* Objective due to eq. (S5) */
11   $\mathit{disable\_dependencies}()$ ;
12   $\mathbf{grad} \leftarrow \nabla_{\hat{\mathbf{x}}} Obj_t$ ; /* Update  $\mathbf{grad}$  w.r.t  $\hat{\mathbf{x}}(t)$  via eq. (6) */
13   $\mathbf{g\_grad} \leftarrow \mathbf{g\_grad} + \nabla_{\mathbf{guide}} Obj_t$ ; /* Update  $\mathbf{guide}$  grads (eq. (S3)) */
14 end
15  $\alpha \leftarrow \mathit{calc\_alpha}(\beta)$ ;
16  $\mathbf{grad} \leftarrow \mathbf{grad} * \sqrt{\alpha(t^*)}$ ; /* Loss grad w.r.t.  $\mathbf{x}$  (eq. (2)) */
17  $\mathbf{g\_grad} \leftarrow \nabla_{\mathbf{x}} \sum (\mathbf{guide} \odot \mathbf{g\_grad})$ ; /* Guidance grad w.r.t.  $\mathbf{x}$  (eq. (S4)) */
18  $\mathbf{grad} \leftarrow \mathbf{grad} + \mathbf{g\_grad}$ ; /* Merge both paths */
19 return  $\mathbf{grad}$ 

```

---

The procedure begins by creating a variable  $\mathbf{g\_grad}$  and setting it to  $\mathbf{0}$  (line 2). This will later be used to store the guidance gradients (see Supplemental B.1). For each time step  $t$  (i.e., step  $i$ ), starting from  $t' = -dt$  ( $i = 1$ ), the process (lines 3-14) first retrieves  $\hat{\mathbf{x}}(t)$  from the saved state  $\mathcal{S}$  (line 4) and the corresponding random noise for that step used during forward propagation (line 5) and computes  $\hat{\mathbf{x}}(t + dt)$ , denoted as  $\hat{\mathbf{x}}_{+dt}$  (lines 7-9). Importantly, these computations are performed while storing graph dependencies (enabled on line 6 and re-disabled on line 11 to restore the normal execution state). Specifically, during the first step, we calculate  $\hat{\mathbf{x}}(0)$  from  $\hat{\mathbf{x}}(-dt)$ . Afterward, we compute the objective  $Obj_t$  (line 10) following eq. (S5) that allows us to back-propagate the gradient from  $\hat{\mathbf{x}}(0)$  to  $\hat{\mathbf{x}}(-dt)$  and  $\mathbf{guide}$  using the stored dependencies, as per eq. (6) and eq. (S2).  $\mathbf{grad}$  is then updated to hold the gradient of the loss function w.r.t.  $\hat{\mathbf{x}}(-dt)$  as desired (line 12), and the gradient of  $\mathbf{guide}$  due to this guidance path (i.e., from  $\mathbf{guide}$  to the loss due to  $\mathbf{guide}$  participating directly in the calculation of  $\hat{\mathbf{x}}(t + dt)$ — see Supplemental B.1) is added to  $\mathbf{g\_grad}$  (line 13). This process repeats until  $\mathbf{grad}$  finally holds the gradient w.r.t.  $\hat{\mathbf{x}}(t^*)$  and  $\mathbf{g\_grad}$  holds the sum of gradients due to all guidance paths w.r.t.  $\mathbf{guide}$  (eq. (S3)). Note that after the required gradients w.r.t.  $\hat{\mathbf{x}}(t)$  and  $\mathbf{guide}$  are obtained at each step, the dependencies are

no longer needed and can be discarded. This is where our approach differs from traditional backpropagation algorithms, enabling memory-efficient gradient calculations (at the cost of an additional forward propagation in total). At this point (line 14), we have the gradient  $\nabla_{\hat{\mathbf{x}}(t^*)} F$  and all that is required is to use it to calculate  $\nabla_{\mathbf{x}} F$ , which is trivial due to the chain rule since the closed-form solution for  $\hat{\mathbf{x}}(t^*) \equiv \mathbf{x}(t^*)$  from eq. (2) indicates that this is equivalent to  $\nabla_{\mathbf{x}} F = \sqrt{\alpha(t^*)} * (\nabla_{\hat{\mathbf{x}}(t^*)} F)$  as we compute on line 16. We then calculate the guidance paths’ gradient w.r.t  $\mathbf{x}$  following eq. (S4) on line 17. Finally, we sum both components, returning the precise full gradient w.r.t.  $\mathbf{x}$ .

## C. Details on Our Low-Frequency (LF) Adversarial Optimization Strategy

### C.1. Understanding Optimizable Filters

In practice, *OFs* extend an advanced class of filters, namely *guided* filters, that improve upon the basic filters discussed in §4.3. *Guided* filters employ additional per-pixel *color kernels* that modulate the distortion at critical points: Since filters interpolate each pixel with its neighbors, they are destructive at edges (intersections between different objects in the image), while the values of non-edge pixels are similar to their neighbors, making such operations of little effect on them. Depending on a permissiveness  $\sigma$ , *guided* filters construct, for each pixel  $(i, j)$  a *color kernel*  $\mathbf{c}_{\mathbf{x}, \sigma_c}^{i,j}$  of the same dimensionality  $M \times N$  as  $\mathcal{K}$  that assigns a multiplier for each of  $(i, j)$ ’s neighbors, that decays with the neighbor’s difference in value from  $(i, j)$ ’s. The output at  $(i, j)$  involves calculating the effective kernel  $\mathbf{v}_{\mathbf{x}, \mathcal{K}, \sigma_c}^{i,j} = \mathbf{c}_{\mathbf{x}, \sigma_c}^{i,j} \odot \kappa$  (normalized) which then multiplies  $(i, j)$ ’s vicinity, taking the sum of this product. Thus, contributions from neighbors whose values differ significantly are diminished, better preserving information.

*Guided* filters still employ the same  $\mathcal{K}$  for all pixels, changing only the *color kernel* that is computed similarly for all pixels. Thus, to incur sufficient changes, they would also require destructive parameters despite them still potentially performing better compared to their pristine counterparts. Their parameters are also predetermined, making it impossible to optimize them for a specific purpose. The *OFs* by Kassis and Hengartner [27] build upon *guided* filters but differ in two ways: First, instead of using the same  $\mathcal{K}$ , they allow each pixel to have its own kernel  $\mathcal{K}^{i,j}$  to better control the filtering effects at each point, ensuring visual constraints are enforced based on each pixel’s visual importance. In this setting,  $\mathcal{K}^*$  denotes the set including all the per-pixel kernels  $\mathcal{K}^{i,j}$ . Second, the parameters  $\theta_{\mathcal{K}^*}$  of each filter are learnable using feedback from a perceptual metric (*lpips*) [65] that models the human vision, leading to an optimal assignment that ensures similarity while maximizing the destruction at visually non-critical regions. To further guarantee visual similarity, they also include *color kernels* similar to *guided* filters (see original paper for details [27]).

### C.2. Attack Hyperparameters

Through experimentation, we found that the loss balancing constants  $c = 10^8$  for *CIFAR-10* and  $c = 10^4$  for *ImageNet* lead to the fastest convergence rates and selected these values accordingly (although other choices are also possible). *UnMarker*’s filter network architecture for *ImageNet* is identical to that from the original paper [27]. For *CIFAR-10*, since the images are much smaller, we found the original architecture unnecessarily costly and often prevents convergence since larger filters group pixels from distant regions together in this case, easily violating visual constraints upon each update, resulting in the *lpips* condition being violated. Thus, we opt for a more compact network that includes filters with smaller dimensions, which was chosen based on similar considerations to [27], allowing us to explore several interpolation options. The chosen architecture for *CIFAR-10* includes 4 filters, whose dimensions are: (5, 5), (7, 7), (5, 5), (3, 3). We use fixed learning rates of 0.008 for the direct modifier  $\delta$  and 0.05 for the filters’ weights, optimized using *Adam*. The remaining hyperparameters were left unchanged compared to [27].

### C.3. Pseudo-Code

The pseudo-code for our low-frequency (*LF*) strategy (see §4.3) is in Algorithm 3. Importantly, as each  $\mathcal{K}_b^{i,j}$ ’s values should be non-negative and sum to 1, the values for each such per-pixel kernel are effectively obtained by *softmaxing* the learned weights. Initially, the modifier  $\hat{\delta}$  is initialized to  $\mathbf{0}$  and the weights  $\{\hat{\theta}_{\mathcal{K}_b^*}\}$  are selected s.t. the filters perform the identity function (line 1). As a result, the attack starts with  $\mathbf{x}_{adv} = \mathbf{x}$  that is iteratively optimized. Similar to C&W [5], we directly optimize  $\mathbf{x}_{adv}$  (i.e., using the modifier  $\hat{\delta}$ ) in the *arctanh* space, meaning we transform the sample first to this space by applying *arctanh* (after scaling  $\mathbf{x}_{adv}$  to *arctanh*’s valid range  $[-1, 1]$ ) where  $\hat{\delta}$  is added and then restore the outcome to the original problem space (i.e.,  $[\min\_val, \max\_val]$ , which is typically  $[0, 1]$ ) via the *tanh* operation. Further details on this method and its benefits can be found in [5]. All other steps correspond to the description brought in §4.3. Unlike §4.1, we assume the classifier  $\mathcal{M}$  outputs the logit vector rather than the probabilities (i.e., we omit the *softmax* layer over its output, which may or may not be re-introduced by the loss  $\ell$ ), as is traditionally done for a variety of

---

**Algorithm 3:** Low-Frequency (*LF*) Adversarial Optimization

---

**Input:** Sample  $x$ , Model (classifier)  $\mathcal{M}$ , *DBP* pipeline  $D$ , Loss function  $\ell$ , True label  $y$  of  $x$ , Perceptual loss  $lpips$ ,  $lpips$  threshold  $\tau_p$ , Filter architecture  $\frac{B}{O_F}$ , Balancing constant  $c$ , Iterations  $max\_iters$ , Success condition  $Cond$ , Filter weights learning rate  $lr_{O_F}$ , Modifier learning rate  $lr_\delta$ , Number of purified copies  $n$ , Number of *EoT*  $eot\_steps$ , Input range limits  $min\_val$ ,  $max\_val$

```
1  $\{\widehat{\theta}_{\mathcal{K}_b^*}\} \leftarrow identity\_weights(\frac{B}{O_F}), \widehat{\delta} \leftarrow \mathbf{0};$  /* Init. attack params. */
2  $Optim \leftarrow Adam([\{\widehat{\theta}_{\mathcal{K}_b^*}\}, \widehat{\delta}], [lr_{O_F}, lr_\delta]);$ 
3  $x_{inv} \leftarrow inv\_scale\_and\_arctanh(x, \backslash$  /* Scale  $x$  to  $[-1, 1]$  and
4  $min\_val, max\_val);$  take  $arctanh$  */
5 for  $i$  in  $1, 2, \dots, max\_iters * eot\_steps$  do
6 |  $x_{adv} \leftarrow \frac{B}{O_F}(tanh\_and\_scale(x_{inv} + \widehat{\delta}, \backslash$  /* Generate adv. using new
7 |  $min\_val, max\_val));$   $\{\widehat{\theta}_{\mathcal{K}_b^*}\}$  and  $\widehat{\delta}$  via eq. (7),
/* scaled to  $[min\_val, max\_val]$  */
8 |  $dist \leftarrow lpips(x, x_{adv});$  /* Calc. perceptual distance */
9 |  $\widehat{x}_{adv}^0 \leftarrow D(repeat(x_{adv}, n));$  /* Get purified outputs */
10 |  $logits \leftarrow \mathcal{M}(\widehat{x}_{adv}^0);$  /* Compute model output */
11 | if  $Cond(logits, y)$  and  $dist \leq \tau_p$  then
12 | | return  $x_{adv};$  /* Success. Return  $x_{adv}$ . */
13 | end
14 |  $Objective \leftarrow \ell(logits, y) + c \cdot max(dist - \tau_p, 0);$  /* Loss via eq. (7) */
15 |  $Objective.backward();$  /* Get grads for  $\{\widehat{\theta}_{\mathcal{K}_b^*}\}$  and  $\widehat{\delta}$  */
16 | if  $i \% eot\_steps = 0$  then
17 | |  $Optim.step();$  /* Update params. */
18 | |  $Optim.zero\_grad();$  /* Reset gradients. */
19 | end
20 end
21 return  $x$  /* Failure. Return original  $x$  */
```

---

adversarial optimization strategies (e.g., C&W [5]) to avoid gradient vanishing. We use the known *max-margin* loss [5]— $\ell(logits, y) = logits[:, y] - \max_{j \neq y} \{logits[:, j]\}$ .

To average the gradients over multiple ( $N$ ) paths as per the adaptive attack’s requirements from §4.1, we generate several purified copies by repeating the sample  $x_{adv}$  under optimization  $n$  times before feeding it into the *DBP* pipeline (line 9). Here,  $n$  corresponds to the maximum number of copies we can fit into the *GPU*’s memory during a single run. However, as this  $n$  may be smaller than the desired  $N$  from §4.1 (i.e., number of *EoT* samples) that allows us to sufficiently eliminate the error in the computed gradient, we use gradient accumulation by only making updates to the optimizable parameters (and then resetting their gradients) every  $eot\_steps$  iterations (lines 16-19). By doing so, the effective number of used copies becomes  $n * eot\_steps$ , which can represent any  $N$  of choice that is divisible by  $n$ . Note that if  $n$  is not a divisor of  $N$ , we can always increase  $N$  until this condition is met, as a larger  $N$  can only enhance the accuracy). This also explains why the algorithm runs for  $max\_iters * eot\_steps$  (line 5).

Finally, the condition  $Cond$  captures the threat model (either *SP* or *MV*— see §3): When the logits for the batch of  $n$  copies are available together with the target label  $y$ ,  $Cond$  outputs a success decision based on whether we seek misclassification for the majority of these purified copies or a single copy only. Note that, as explained in §5.3, we take the majority vote over the maximum number of copies we can fit into the *GPU* (i.e.,  $n$ ) for *MV*. As this choice was only made for practical considerations, one may desire to experiment with different configurations wherein another number of copies is used. Yet, this is easily achievable by simply modifying  $Cond$  accordingly: For instance, we may augment it with a history that saves the output logits over all  $eot\_steps$  (during which  $x_{adv}$  is not updated). Then, the majority vote can be taken over all copies in this window. Note that by increasing the number of  $eot\_steps$ , we can use as many copies for the majority vote decision as desired in this case. That said, the attack will become significantly slower.

In addition to the precise gradient module **DiffGrad**, our *DiffBreak* toolkit provides the implementation of our *LF* strategy



as well as various other common methods (e.g., *AutoAttack* and *StAdv*), to enable robust and reliable evaluations of *DBP*. All strategies are optimized for performance to speed up computations via various techniques such as just-in-time (*JIT*) compilation. Our code is available at <https://github.com/andrekkassis/DiffBreak.git>.

## D. Verifying The Correctness of Our DiffGrad Module

All that is required to ensure the fidelity of our module is to guarantee that each  $\hat{x}(t + dt)$  computed during back-propagation (line 9 in Algorithm 2) matches exactly  $\hat{x}(t + dt)$  calculated during forward propagation (line 14 in Algorithm 1). With that verified, the module’s state simulates that created by automatic differentiation engines during their normal operation, and we can rely on their correctness from that point onward, as we use them to perform the necessary back-propagation between each  $\hat{x}(t + dt)$  and  $\hat{x}(t)$ . Since we have access to the state  $S$  that stores the forward propagation’s intermediate outputs, we can retrieve this original  $\hat{x}(t + dt)$  from  $S$  at each step  $t$  during backpropagation and compare it to the newly calculated value. If the results match exactly, then we know our algorithm is computing the exact gradients. We manually verified this requirement for each  $t$ , providing the first-ever reliable module for this task. Note that the validity of the additional guidance gradients we include can be ensured by verifying the derivation presented in Supplemental B.1. Then, the same steps presented thus far in this section ensure practical correctness.

## E. Re-evaluating DiffAttack in The Presence of Precise Gradients

**DiffAttack** [26] employs the *per-step* losses discussed in §5 to influence the score model’s behavior, causing *DBP*’s output distribution to diverge from the natural one. Yet, as we demonstrated in §4.1 that the adaptive attack alone already targets this objective in a manner that also directly aims for misclassification (rather than simply altering the output distribution indifferently), **DiffAttack**’s *per-step* losses that fail to do so become sub-optimal and redundant. This explains our **Full-DiffGrad**-based adaptive attack’s (i.e., that only uses the accurate loss gradients) superior performance in §5.2 compared to **DiffAttack**’s previously-reported results [26]. We further claim that due to this discrepancy in objectives, **DiffAttack**’s *per-step* losses can negatively impact its performance even if this same technique were optimized to use the accurate gradients as well. This is because when the two objectives— misclassification and general divergence from the natural distribution— do not align, the *per-step* losses introduce additions to the optimal gradients that cause the input to move in an unwanted direction. This is despite their benefits when the exact gradients are not accessible (due to the previous implementation errors) as the two objectives are similar, causing these *per-step* losses, despite their sub-optimality, to potentially apply useful corrections to the faulty back-propagated gradients along the reverse path, explaining the findings of the original paper [26].

To prove this claim, we conduct the same experiment from §5.2, which evaluates the robustness against the *AutoAttack*- $\ell_\infty$  strategy (with  $\epsilon_\infty = 4/255$ ) under *SP*, on *ImageNet*’s *DiffPure*-protected DeiT-S classifier with **DiffAttack** that we adapt to instead use the accurate gradients as well (via our gradient module). We then compare its performance with the optimized adaptive attack (i.e., **Full-DiffGrad**-based) considered in the paper that only uses the accurate gradients without **DiffAttack**’s *per-step* losses. This enhanced version of **DiffAttack** achieves Rob-Acc of 25%, which is an improvement over the authors’ version (32.81%) but worse than the 21.09% obtained by our **Full-DiffGrad**-based attack (see §5.2). This defies the theory presented in the original paper and the claimed vast improvement attributed to the *per-step* losses. Under *MV* and with the same configuration, **DiffAttack**’s disadvantages become more evident, yielding Rob-Acc of 42.21%, which is drastically worse compared to our **Full-DiffGrad**-based attack (32.81%— see §5.3). Upon repeating these experiments for *CIFAR-10*’s WideResNet-70-16 (with  $\epsilon_\infty = 8/255$ ), we find **DiffAttack** does lower the Rob-Accs, attaining 8.14% under *SP* (compared to the 17.58% we report in §5.2), which is a total improvement of 9.44%. Still, this advantage is well below the gain reported by the authors [26], wherein **DiffAttack** improved upon the **adjoint** method by 25.98%. Worse yet, under *MV*, **DiffAttack** only lowers WideResNet-70-16’s Rob-Acc by 2.76% to 44.96% (in comparison, the **Full-DiffGrad**-based attack reaches 47.72% in §5.3), making its impact in this stricter setting insignificant.

The most probable explanation for **DiffAttack**’s slightly improved results against *CIFAR-10*’s WideResNet-70-16 is that the **Full-DiffGrad**-based attack may get stuck at a local minimum, preventing further progress. Since **DiffAttack**’s *per-step* losses interfere with the gradients, they might force the optimization procedure to step outside of the environment of this stationary point, which could lead to convergence to a better solution. Yet, as observed for *ImageNet*, the performance gain is contingent on whether these *per-step* losses’ objective of arbitrarily altering *DBP*’s output distribution directly translates to misclassification. While this seems to hold for *CIFAR-10*’s WideResNet-70-16, the degraded performance against *ImageNet*’s DeiT-S proves this assumption does not apply universally. Moreover, as the potential improvement with *DiffAttack* is only the product of avoiding local minima, its benefits are far rarer than previously thought [26], as can be seen above. This same outcome can also be easily achieved by expanding the search space around the original sample (e.g., by using a more

permissive optimization strategy such as *LF*— see §5.4), making **DiffAttack**’s additional components unnecessary at best.

All in all, **DiffAttack** can be destructive in the worst case, resulting in a performance degradation compared to the standard adaptive attack alone (with the correct gradients). In the instances where it boosts the performance, it is far less advantageous than originally thought, with its drawbacks outweighing its benefits in total (i.e., when averaging over both evaluated classifiers and the two threat models) and especially in the challenging *MV* setup. Thus, we find **DiffAttack** counter-productive and recommend the **Full-DiffGrad**-based attack instead.

## F. Example Attack Images

In Supplemental F.1-F.10, we provide a variety of successful attack images that cause misclassification in the rigorous *MV* setting, generated using our low-frequency (*LF*) strategy against all systems considered in §5.4. For the configurations that were also evaluated against *AutoAttack- $\ell_\infty$*  under *MV* in §5.3, we include successful samples generated with this method as well for comparison. Note that all samples are crafted using the parameters listed in §5.3 and §5.4. That is,  $\tau_p = 0.05$  for *LF* and  $\epsilon_\infty = 8/255$  for *AutoAttack* against *CIFAR-10* and  $\epsilon_\infty = 4/255$  against *ImageNet*. For the configurations that were evaluated against both strategies, we provide two sets of samples: 1) Three triplets containing the original image, the *AE* generated using *AutoAttack*, and the *AE* crafted using *LF*. Importantly, all original samples in this set are inputs for which both methods can generate successful *AEs*, and we provide these to allow for a direct comparison between the two strategies’ output quality on a sample-by-sample basis. Yet, as *AutoAttack* is inferior to our approach (*LF*), resulting in the systems retaining robustness on many inputs for which it fails to generate successful *AEs* under *MV*, it is essential to inspect *LF*’s outputs on such more challenging samples to demonstrate that it still preserves quality despite its ability to fool the target classifiers. Thus, we include a second set of 2) Three successful *AEs* generated with *LF* from inputs on which *AutoAttack* fails under *MV*. For the remaining configurations that were not evaluated against *AutoAttack* under *MV* in 5.3, we provide six successful *AEs* generated with *LF*.

In Supplemental F.11, we present attack images generated by the non-norm-bounded *StAdv* [54] strategy. This method has demonstrated superior performance to norm-based techniques in the past against *DBP* [36] even in the absence of the correct exact gradients, indicating it could be a viable attack strategy with our gradient computation fixes, thereby making our *LF* approach unnecessary. Yet, previous evaluations only considered *StAdv* against *DBP* for *CIFAR-10* [36]. While we find *StAdv* capable of defeating all systems (for both *CIFAR-10* and *ImageNet*), it leads to severe quality degradation when used to attack *DBP*-protected classifiers for high-resolution inputs (i.e., *ImageNet*), leaving the *AEs* of no utility. Thus, we deem it unsuitable, excluding it from the main body of the paper accordingly. Further details are in Supplemental F.11.

All samples below are originally (without adversarial perturbations) correctly classified.

### F.1. Attack Samples Generated Against *CIFAR-10*’s WideResNet-70-16 with *GDMP* Purification

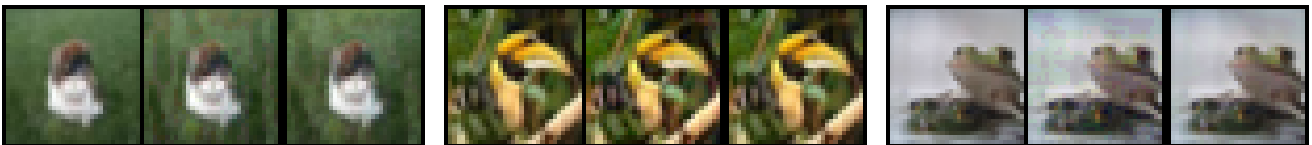


Figure S1. Successful attacks generated by *LF* and *AutoAttack- $\ell_\infty$* . Left - original image. Middle - *AutoAttack*. Right - *LF*.

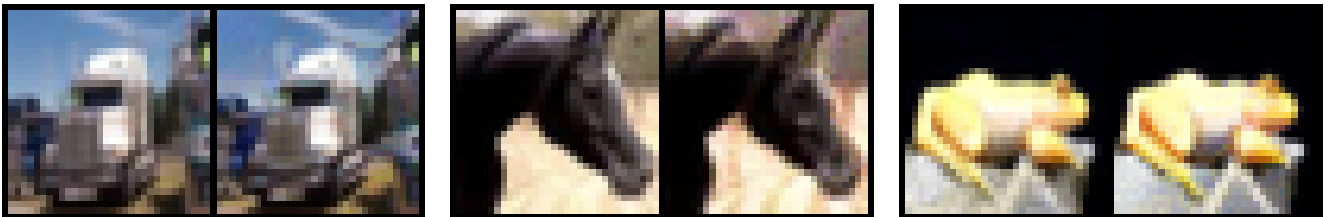


Figure S2. Successful *LF* attacks on inputs for which *AutoAttack- $\ell_\infty$*  fails. Left - original image. Right - *LF*.

## F.2. Attack Samples Generated Against *CIFAR-10*'s WideResNet-28-10 with *GDMP* Purification



Figure S3. Successful attacks generated by *LF* and *AutoAttack- $\ell_\infty$* . Left -original image. Middle - *AutoAttack*. Right - *LF*.

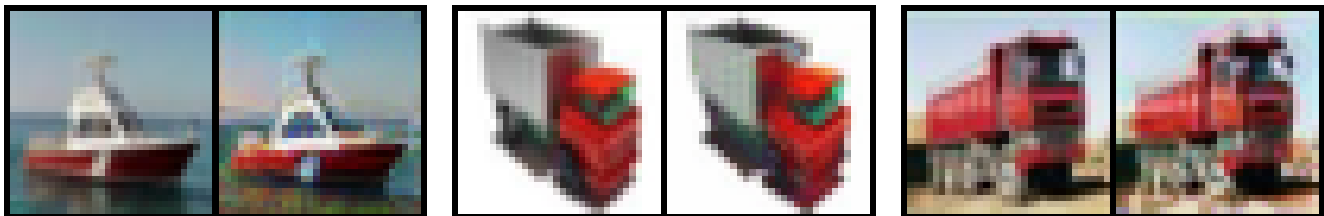


Figure S4. Successful *LF* attacks on inputs for which *AutoAttack- $\ell_\infty$*  fails. Left - original image. Right - *LF*.

## F.3. Attack Samples Generated Against *CIFAR-10*'s WideResNet-70-16 with *DiffPure* Purification

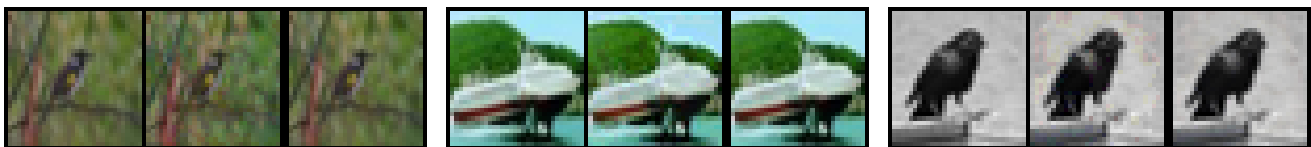


Figure S5. Successful attacks generated by *LF* and *AutoAttack- $\ell_\infty$* . Left -original image. Middle - *AutoAttack*. Right - *LF*.

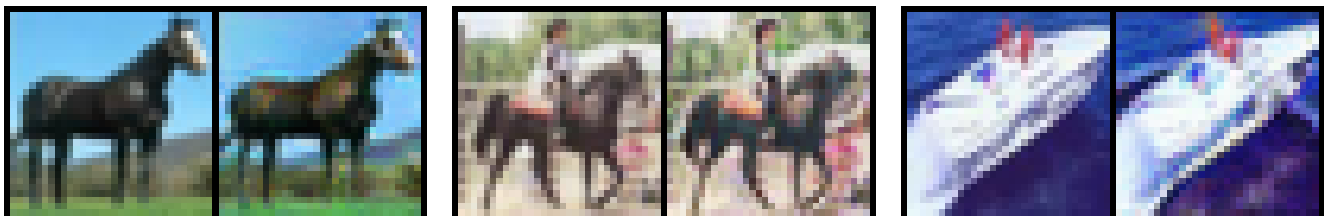


Figure S6. Successful *LF* attacks on inputs for which *AutoAttack- $\ell_\infty$*  fails. Left - original image. Right - *LF*.

#### F.4. Attack Samples Generated Against *CIFAR-10*'s WideResNet-28-10 with *DiffPure* Purification



Figure S7. Successful attacks generated with *LF*. Left -original image. Right - *LF*.

#### F.5. Attack Samples Generated Against *ImageNet*'s DeiT-S with *GDMP* Purification



Figure S8. Successful attacks generated by *LF* and *AutoAttack- $\ell_\infty$* . Left -original image. Middle - *AutoAttack*. Right - *LF*.



Figure S9. Successful  $L_F$  attacks on inputs for which  $AutoAttack-l_\infty$  fails. Left - original image. Right -  $L_F$ .

### F.6. Attack Samples Generated Against *ImageNet*'s WideResNet-50-2 with *GDMP* Purification

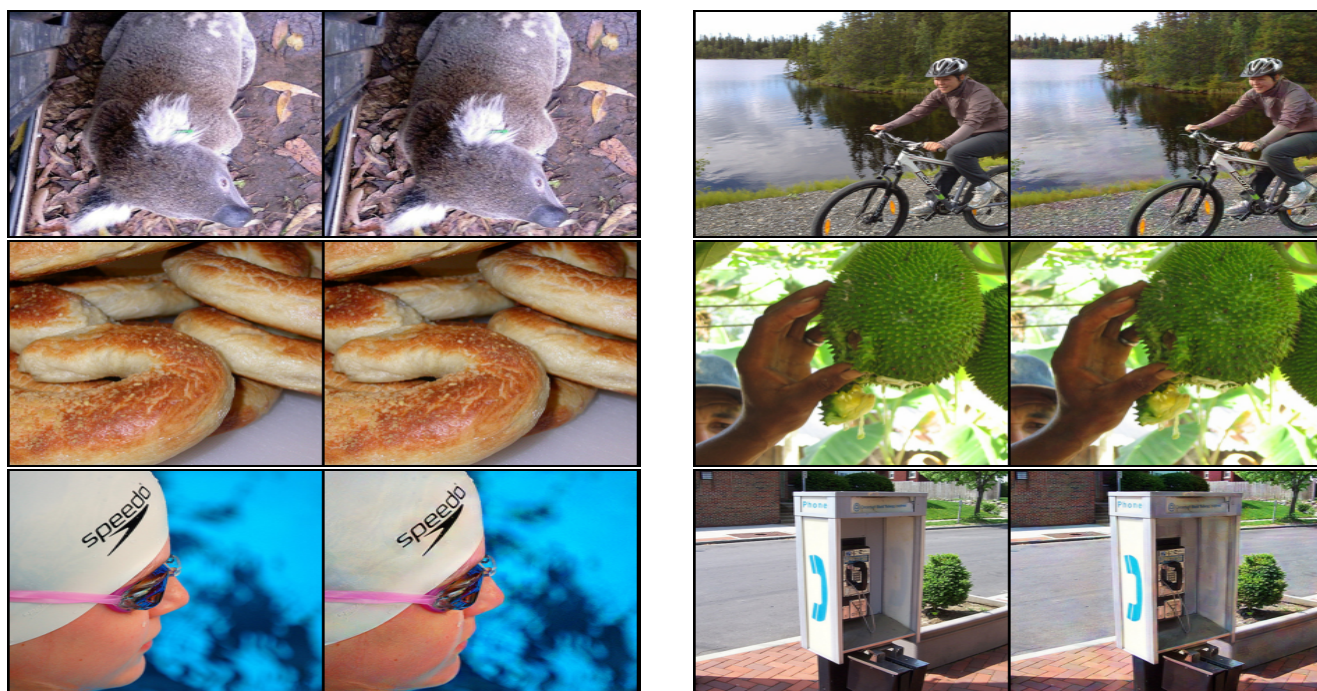


Figure S10. Successful attacks generated with  $L_F$ . Left - original image. Right -  $L_F$ .

**F.7. Attack Samples Generated Against *ImageNet*'s ResNet-50 with *GDMP* Purification**



Figure S11. Successful attacks generated with *LF*. Left -original image. Right - *LF*.

**F.8. Attack Samples Generated Against *ImageNet*'s DeiT-S with *DiffPure* Purification**



Figure S12. Successful attacks generated by *LF* and *AutoAttack- $l_\infty$* . Left -original image. Middle - *AutoAttack*. Right - *LF*.

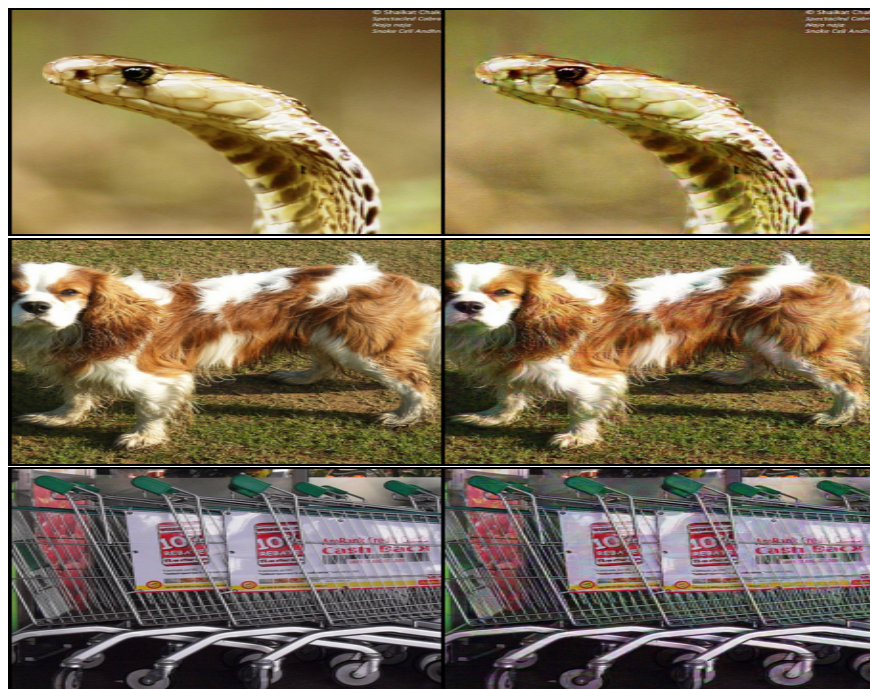


Figure S13. Successful  $LF$  attacks on inputs for which  $AutoAttack-\ell_\infty$  fails. Left - original image. Right -  $LF$ .

### F.9. Attack Samples Generated Against *ImageNet*'s WideResNet-50-2 with *DiffPure* Purification

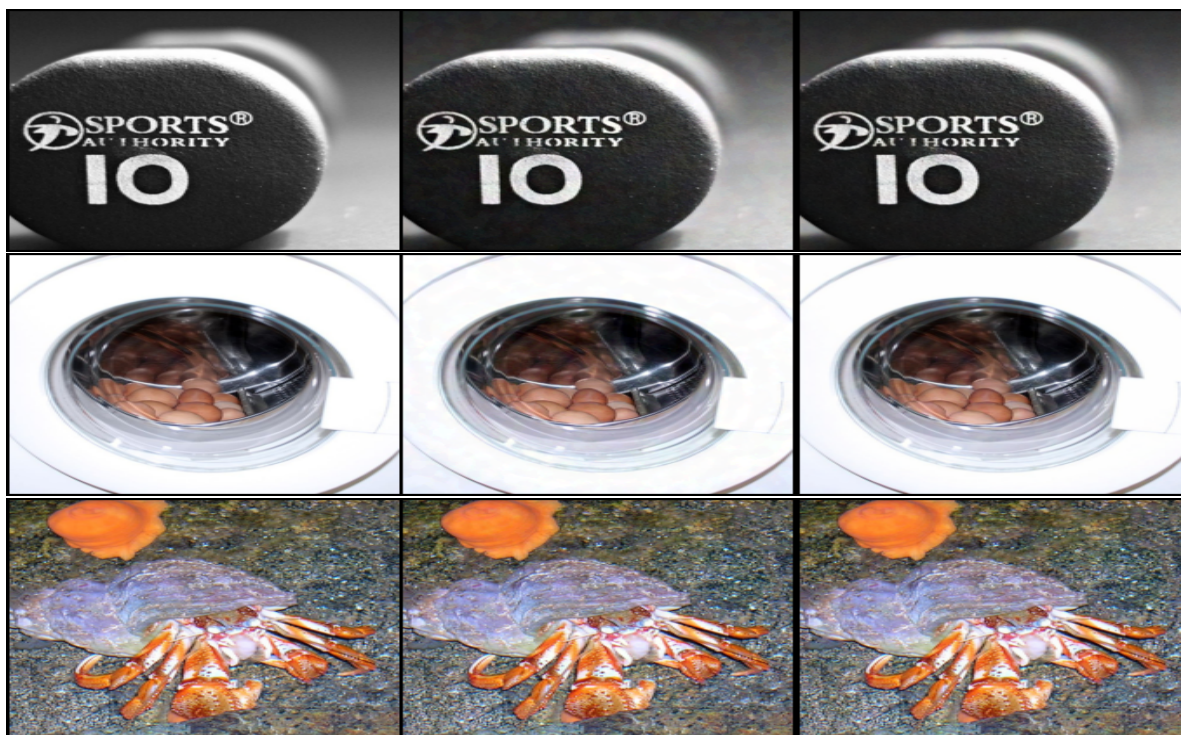


Figure S14. Successful attacks generated by  $LF$  and  $AutoAttack-\ell_\infty$ . Left - original image. Middle -  $AutoAttack$ . Right -  $LF$ .

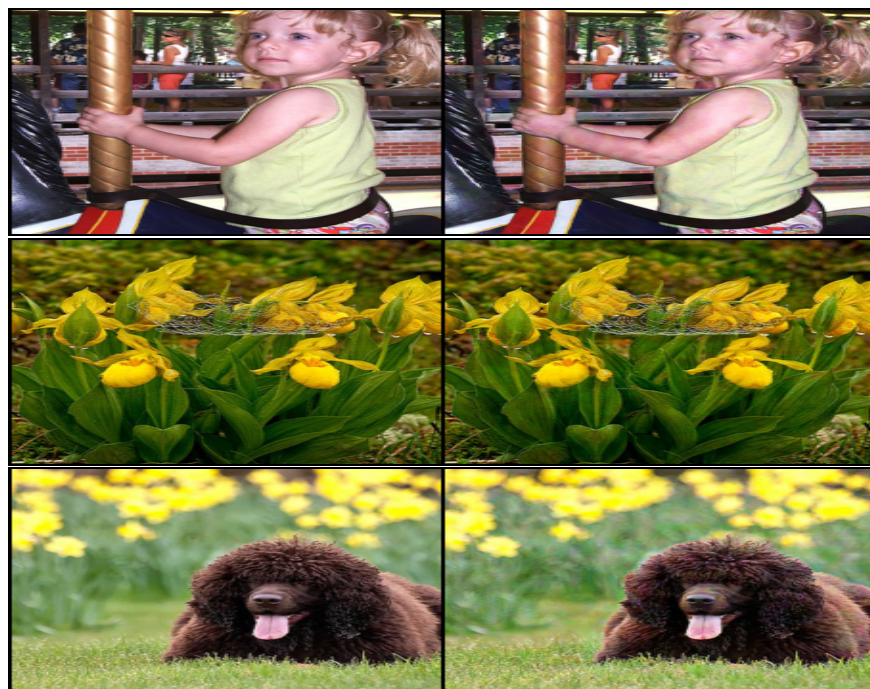


Figure S15. Successful  $LF$  attacks on inputs for which  $AutoAttack-\ell_\infty$  fails. Left - original image. Right -  $LF$ .

### F.10. Attack Samples Generated Against *ImageNet*'s ResNet-50 with *DiffPure* Purification



Figure S16. Successful attacks generated with  $LF$ . Left - original image. Right -  $LF$ .



### F.11. Quality Comparison with *StAdv*

We found *StAdv* capable of generating outputs that defeat *DBP* even under *MV*. However, it is not suitable for targeting *DBP*-defended classifiers that operate on high-resolution images. The reason is that *StAdv* performs spatial transformations that relocate the different pixels. Thus, its changes quickly become visible when applied excessively. Due to the considerable stochasticity of *DBP* (see §5.3), the required displacements (especially in the *MV* setting) are significant, which in turn can severely impact the quality. For low-resolution inputs (e.g., *CIFAR-10*), *StAdv* can still be effective, with the quality degradation remaining unnoticeable due to the size of the images that renders them blurry by default, masking *StAdv*'s effects. For high-resolution inputs, the degradation is substantial, leaving the outputs useless as stealthiness is a key requirement from practical *AEs* [27]. *StAdv*'s successfully misclassified samples (under *MV*) below prove these claims. We use **Full-DiffGrad** for backpropagation and run *StAdv* with its default parameters [54]. When the parameters are changed to better retain quality, *StAdv* ceases to converge for *ImageNet*, making it of no use. All provided samples are originally correctly classified.

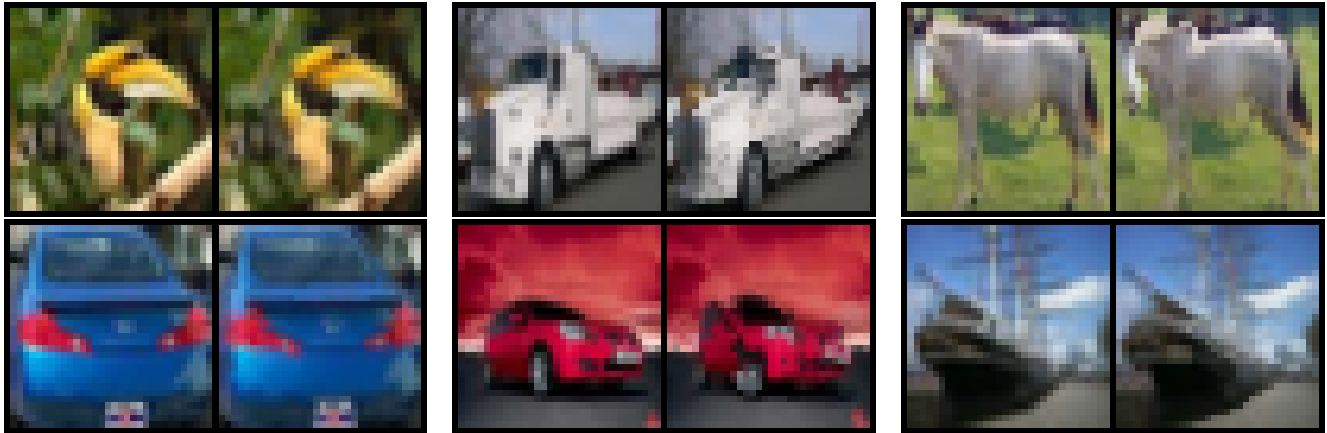


Figure S17. *StAdv* attacks against *CIFAR-10*'s WideResNet-70-16 with *GDMP* purification. Left - original image. Right - *StAdv*.

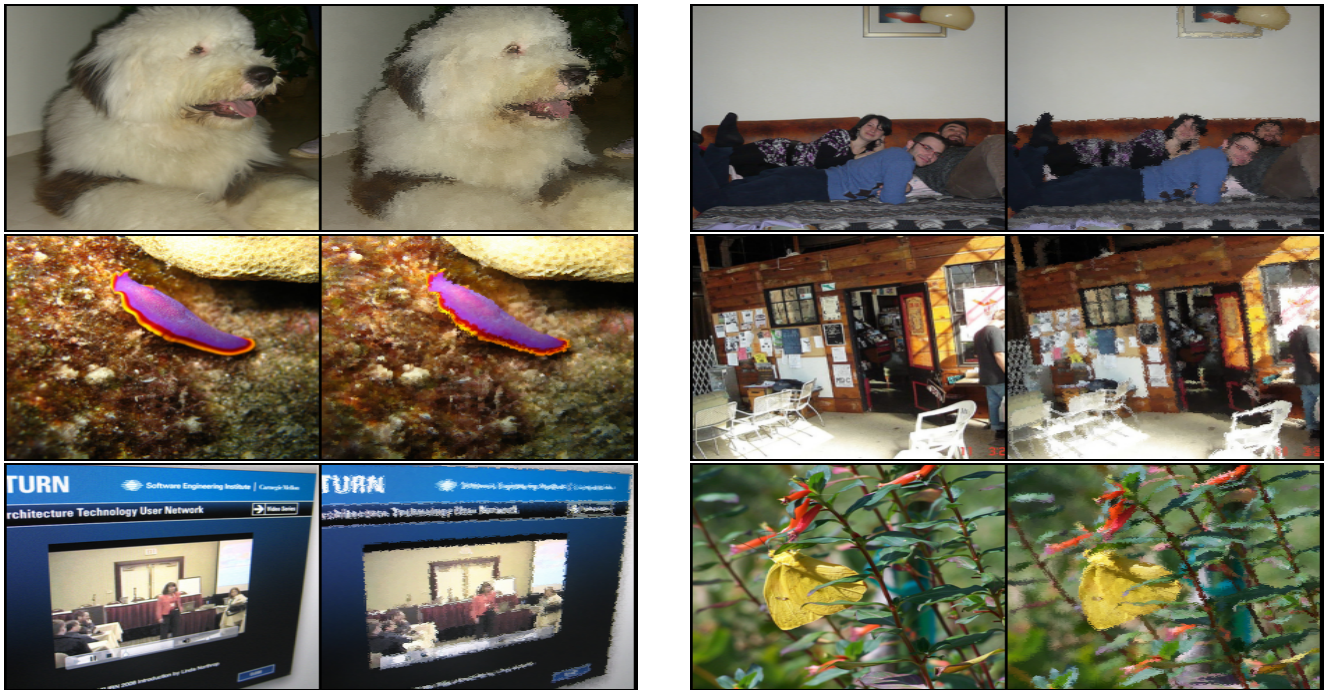


Figure S18. *StAdv* attacks against *ImageNet*'s DeiT-S with *DiffPure* purification. Left - original image. Right - *StAdv*.